PAPER

ZIF-67/CQD nanohybrids for combined adsorptive and photocatalytic removal of tetracycline: kinetic, isotherm, and mechanistic insights

Khizra Ali,†[a] Palkaran Sethi†[b] and Soumen Basu [ID] *[b]

The uncontrolled dissemination of antibiotic residues in aquatic environments necessitates the development of multifunctional materials capable of efficiently eliminating such pollutants through synergistic mechanisms. In this investigation, a series of zeolitic imidazolate framework (ZIF-67)/carbon quantum dot (CQD) nanohybrids were fabricated *via* a facile solvothermal strategy by modulating the CQD loading (5%, 10%, and 15% w/w) to optimize their adsorption and photocatalytic efficiencies toward tetracycline remediation. Structural, morphological, and physicochemical attributes were meticulously elucidated through X-ray diffraction (XRD), Fourier transform infrared (FTIR) spectroscopy, field-emission scanning electron microscopy (FESEM), energy-dispersive X-ray spectroscopy (EDS), Brunauer–Emmett– Teller (BET) surface area analysis, photoluminescence spectroscopy (PL), ultraviolet-visible diffuse reflectance spectroscopy (UV-vis DRS), and X-ray photoelectron spectroscopy (XPS), confirming the high crystallinity, uniform CQD dispersion, enlarged surface area, and improved charge-transfer dynamics of the composites. Among the synthesized samples, the 10ZQ (10% w/w CQD-loaded ZIF-67) composite exhibited the most pronounced performance, achieving 99% removal of 50 ppm tetracycline within 50 min under sunlight irradiation, corresponding to an apparent rate constant of $k = 0.0057$ min^{-1}. Adsorptive behavior was evaluated through comprehensive modeling using Langmuir, Freundlich, Temkin, Harkins–Jura, Halsey, and Dubinin–Radushkevich isotherms, along with kinetic models, including pseudo-first-order, pseudo-second-order, Elovich, liquid-film diffusion and intraparticle diffusion equations, and degradation kinetics, including zero-order, pseudo-first-order, and pseudo-second-order kinetics. The adsorption data fit well in the Langmuir model ($R^2 = 0.9916$) and Elovich kinetics model ($R^2 = 0.9977$), indicating homogeneous monolayer chemisorption. Photocatalytic degradation kinetics also closely followed the zero-order model ($R^2 = 0.9932$). Reactive species trapping experiments revealed that superoxide radicals ($\cdot O_2^-$) were the dominant oxidants in tetracycline oxidation. Furthermore, mineralisation analysis showed 76% TOC removal and 78% COD removal, confirming the substantial oxidation of tetracycline into harmless inorganic products. HRMS analysis unveiled the evolution of various intermediates *via* ring-cleavage, demethylation, and hydroxylation reactions, allowing a detailed mechanistic pathway to be proposed. Overall, this work introduces a robust dual-functional ZIF-67/CQD heterostructure exhibiting exceptional stability, recyclability, and activity for antibiotic removal, thereby establishing a promising platform for sustainable wastewater purification.

Sustainability spotlight

Antibiotic contamination in water systems threatens ecosystem integrity and public health, demanding treatment strategies that are both effective and environmentally responsible. This work presents a sustainable ZIF-67/CQD nanohybrid that achieves rapid tetracycline removal through synergistic adsorption and sunlight-driven photocatalysis, enabling 99% elimination with substantial mineralisation and excellent recyclability. By harnessing solar energy, minimizing chemical inputs, and ensuring long-term material stability, this approach reduces energy demand, operational costs, and secondary pollution typically associated with conventional treatment methods. The high efficiency, reusability, and scalability of the system support the advancement of green water purification technologies, directly contributing to UN SDG 6 (Clean Water and Sanitation), SDG 9 (Industry, Innovation, and Infrastructure), and SDG 12 (Responsible Consumption and Production).

[a]*Department of Chemistry, Aligarh Muslim University, Aligarh-202002, India*

[b]*Department of Chemistry and Biochemistry, Thapar Institute of Engineering & Technology, Patiala-147004, India. E-mail: soumen.basu@thapar.edu*

† Both authors have equal contributions.

1. Introduction

Human health and environmental sustainability are seriously threatened by the increasing discharge of newly emerging contaminants (NECs) into aquatic ecosystems.[1] Among these, antibiotics represent one of the most alarming categories of pollutants, primarily due to their extensive and often indiscriminate use in medical, veterinary, and agricultural practices.[2] The exponential rise in the global production and consumption of pharmaceuticals—including insecticides, pesticides, and antibiotics—has resulted in persistent contamination of natural water bodies.[3] By 2023, the global antibiotic utilisation was estimated to reach nearly 128 billion standard daily doses, an increase of almost 200% since 2015, and it is expected to surpass 105 000 tons by 2030. These concerning projections highlight the pressing need for effective and sustainable remediation methods.[4]

Antibiotics, though indispensable in treating bacterial infections in humans, animals, and aquaculture, exhibit high environmental persistence and bioactivity even after excretion.[5] They often enter water systems in their unchanged or partially metabolized forms, posing severe risks to aquatic organisms and public health.[6] Consequently, antibiotics are now recognized as "emerging contaminants" due to their continuous input, recalcitrant nature, and potential to induce antimicrobial resistance (AMR). Notably, AMR-related mortality in the United States alone is projected to surpass the combined fatalities caused by diabetes and cancer, accounting for over 23 000 deaths annually.[7]

Among various antibiotic classes, tetracyclines are the second most widely used group, constituting nearly one-third of the global antibiotic production and consumption.[8] They are especially used in medical and veterinary applications due to their activity against bacteria, protozoan parasites, and mycoplasma.[9] However, approximately 70% of administered tetracyclines are excreted in their active forms, leading to the continuous release of endocrine-disrupting compounds (EDCs) into the aquatic environment, adversely affecting hormonal balance and ecosystem stability.[10]

Traditional methods of treatment such as membrane filtration, ozonation, adsorption, Fenton and photo-Fenton reactions, biological deterioration, electrochemical processes, chlorination and oxidation have been studied for the elimination of antibiotics.[11] Although these methods show certain advantages, their practical applicability is often limited by secondary pollution, high operational costs, incomplete degradation, and complex operating conditions. By contrast, because semiconductor-based photocatalysis can mineralize organic pollutants under light irradiation, it has become a highly effective, environmentally friendly, and sustainable technology for the degradation of antibiotics.[12–14] However, photocatalysis' effectiveness is frequently hindered by charge carriers and restricted surface contact with target molecules.

To overcome these challenges, the integration of adsorption and photocatalysis has gained significant attention as a synergistic approach that combines the preconcentration of pollutants on catalyst surfaces with their subsequent photo-induced degradation. This dual mechanism accelerates pollutant removal, enhances degradation efficiency, and enables *in situ* regeneration of active sites.[15,16] A variety of adsorptive materials, such as carbon-based materials, calcium alginate, polymers,[17] zeolites,[18] and metal–organic frameworks (MOFs),[5] have been scrutinised for such applications.

MOFs are unique among them because of their high surface area, adjustable porosity, and adaptable chemical activity. Because of their exceptional chemical and thermal stability, zeolitic imidazolate frameworks (ZIFs), a subclass of MOFs made up of transition metal ions (such as Co^{2+} and Zn^{2+}) and imidazolate linkers, are perfect for photocatalytic and adsorption-based processes.[19] Recently, there has been a growing interest in combining MOFs with functional nanomaterials, which results in hybrid structures. A Cu-MOF/ZnO composite was created by Roy *et al.* as a potent MOF-based photocatalyst for the degradation of organic dyes in the presence of natural sunlight.[20] A MIL-68 (In)–NH_2/GrO composite was created by Yang *et al.* as a visible light-responsive MOF-based photocatalyst for amoxicillin degradation, exhibiting improved charge separation and stability.[21]

In this context, carbon quantum dots (CQDs) have emerged as promising cocatalysts owing to their outstanding optical properties, high conductivity, upconversion photoluminescence, and ability to act as electron reservoirs.[22] The incorporation of CQDs into MOF structures significantly enhances light absorption and suppresses charge recombination. For instance, Ghasemzadeh *et al.* developed a CQD@MOF-808 guest@host nanocomposite *via* an *in situ* thermolysis route, in which the embedded CQDs enhanced visible-light-driven photocatalytic degradation through improved charge separation and UCPL effects,[23] and Song *et al.* designed a CQD-bridged Bi-MOF@g-C_3N_4 heterojunction (BCC-4), in which the *in situ* embedded CQDs facilitated charge transfer through a built-in electric field, enabling the efficient visible-light-driven degradation of norfloxacin *via* a dual-circulation pathway.[24]

Despite significant progress, most existing photocatalytic materials still exhibit insufficient charge separation, slow degradation kinetics, and inconsistent performance under variable water conditions. Hence, in this study, ascorbic acid-derived CQDs were integrated with ZIF-67 to form novel CQD/ZIF-67 nanocomposites with enhanced photocatalytic and adsorptive characteristics. By tuning the CQD loading ratio (5%, 10%, and 15%), we methodically examined how they affected the final composites' functional, optical, physical and chemical properties. The CQD loadings of 5%, 10%, and 15% were chosen to examine the influence of low, moderate, and high CQD incorporation, respectively, on interfacial charge transfer and light utilization. This range enabled the identification of an optimal loading while avoiding excessive CQD coverage, which may hinder light absorption or block active sites. FTIR, XRD, FESEM, EDS, XPS, BET, UV-vis DRS, and PL studies were used to thoroughly evaluate the produced catalysts in order to verify their crystallinity, shape, stability, and charge transfer behavior. Their adsorption and photocatalytic performances were rigorously assessed through adsorption isotherms, kinetic

Paper

modeling, photocatalytic kinetic analysis, and mechanistic investigations. In addition, TOC, COD, and HRMS studies were performed to elucidate the mineralization efficiency and degradation pathways of tetracycline at a very high initial concentration (50 ppm). This work not only bridges the knowledge gap regarding CQD/ZIF-67-based dual-functional systems but also provides a detailed mechanistic understanding of their synergistic adsorption–photocatalysis process. The findings establish CQD/ZIF-67 as a robust and reusable composite for practical antibiotic removal, offering a promising pathway toward sustainable water purification technologies.

2. Materials and methodology

2.1 Raw materials

High-purity reagents from Loba Chemie Pvt. Ltd, such as cobalt (II) nitrate hexahydrate (98% extra pure), 2-methylimidazole (98% extra pure), and L-ascorbic acid (99% extra pure), were used to synthesize the materials. We purchased a commercial tetracycline powder from Sigma-Aldrich. For all solution preparations, ultrapure double-distilled water was used.

2.2. Synthesis

2.2.1. Synthesis of carbon quantum dots (CQDs). Ascorbic acid was used as the carbon precursor in a straightforward hydrothermal process to prepare carbon quantum dots (CQDs). To ensure thorough dissolution and uniform dispersion, 1 g of ascorbic acid (11.36 mmol) was dissolved in 10 mL of DI water while being constantly mixed. The suspension was subsequently sonicated for 30 minutes at ambient temperature. The resulting transparent solution was transferred into a 50 mL Teflon-lined stainless-steel autoclave and subjected to hydrothermal treatment at 180 °C under self-generated pressure for 8 hours. The autoclave was left to spontaneously cool to ambient temperature once the hydrothermal process was finished. The yellowish solution that was produced showed that carbon quantum dots, or CQDs, were successfully formed, in accordance with a previously documented process.[12]

2.2.2. Synthesis of ZIF-67. ZIF-67 was synthesized using a modified reported method (J. Qian *et al*).[25] Briefly, 0.90 g of $Co(NO_3)_2 \cdot 6H_2O$ (1.55 mmol) was dissolved in 6 mL of DI water, and 2-methylimidazole (Hmim; 11 g, 67 mmol) was independently dissolved in 40 mL of DI water. To guarantee total dissolution, the solutions were sonicated for 30 minutes. The two solutions were then combined while gently swirling, creating a uniform purple solution. To promote crystal formation, the mixture was magnetically agitated for six hours at room temperature. The obtained purple precipitate was harvested *via* centrifugation (8000 rpm, 15 min), rigorously washed with DI water and methanol (three times each) to remove unreacted species, and oven-dried at 90 °C for 24 h to yield pure ZIF-67 (ZF).[26]

2.2.3 Synthesis of CQD/ZIF-67 nanocomposites. A specific amount of CQDs—5.6 mL, 12.4 mL, and 19.8 mL, which corresponded to 5%, 10%, and 15% ratios, respectively—was taken and added to three beakers. In two separate beakers, 0.45 g of

cobalt nitrate hexahydrate in 3 mL of DI water and 5.5 g of 2-methylimidazole in 20 mL of DI water were prepared as precursor solutions. These, along with the first solution, were sonicated for 30 minutes. Afterward, all three were mixed and continuously stirred at room temperature for 6 hours. The obtained solids were centrifuged at 8000 rpm for 15 minutes, washed thoroughly with DI water and methanol (three times each), and dried at 90 °C. The final samples were named as 5ZQ, 10ZQ, and 15ZQ based on their weights, respectively. Scheme 1 shows the synthesis procedure and pictures of the CQD/ZIF-67 hybrid.

2.3 Characterisation methods

The characterisation techniques are listed in the SI S1.

### 2.4 Adsorption and photocatalytic degradation experiments

Sequential adsorption and photocatalytic degradation studies were used to assess the ZQ nanocomposites' dual capability for tetracycline removal. DI water was used to prepare a tetracycline stock solution (1000 ppm), which was then diluted to the required concentrations. A known dosage of the composite (0.1 g L^{-1}) was combined with 20 mL of a 50 ppm tetracycline solution for each experiment, and the mixture was shaken under dark conditions for 45 min to ensure adsorption equilibrium and suppress photolytic effects. All adsorption and photocatalytic degradation experiments were carried out under magnetic stirring at 700 rpm in 30 mL test tubes, with a solution depth of ∼12 cm and the lamp positioned at a distance of 10 cm from the test tubes. Under these conditions, the ZQ nanocomposites exhibited an adsorption behaviour toward tetracycline, confirming the effective preconcentration of the pollutant on the catalyst surface prior to light irradiation. Subsequently, the suspension was centrifuged, and the remaining tetracycline in the supernatant was determined at 357 nm *via* UV-vis spectrophotometry. eqn (1) was used to obtain the removal efficiency (*R*%):

$$R\% = \frac{C_{initial} - C_{final}}{C_{initial}} \times 100 \quad (1)$$

where $C_{initial}$ and C_{final} are the initial and equilibrium tetracycline concentrations, respectively. Experiments were executed in triplicate, and the corresponding mean values were reported. These adsorption–desorption equilibrium results were used as the baseline to distinguish between adsorption-driven removal and photocatalytic degradation.

An identical tetracycline-composite suspension was exposed to photocatalytic degradation in the presence of sunlight after adsorption. Photocatalytic degradation experiments were primarily carried out under natural sunlight to evaluate real-world applicability; additionally, comparative studies were performed using a 40 W LED lamp and a UV light source (365 nm) under identical experimental conditions to enable comparison. Tetracycline degradation was tracked using UV-vis spectroscopy at 357 nm after samples were removed at prearranged intervals and centrifuged to eliminate the catalyst. Different parameters, including dose, light source, initial
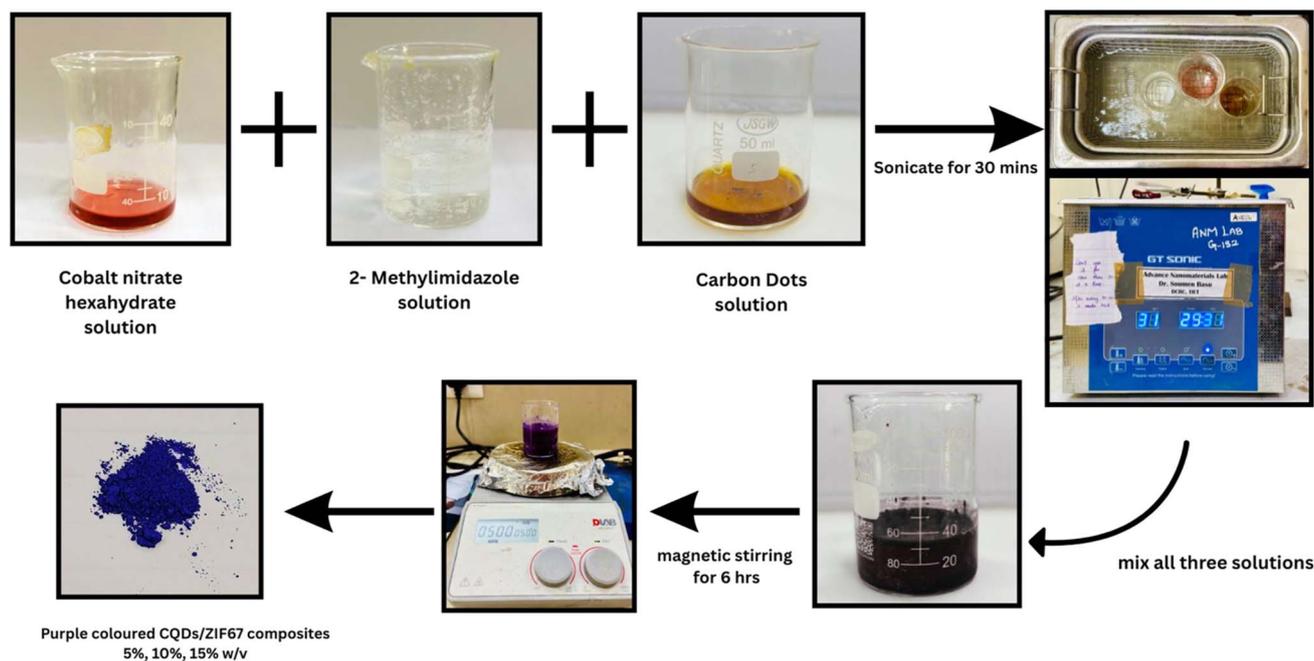
Scheme 1 Schematic of the synthetic procedure for CQD/ZIF-67 nanocomposites.

concentration, and pH, were optimised to obtain the best removal percentage. Further, these data were used to plot different isotherms and kinetic models, which were used to extract the rate constants.

To assess the extent of mineralisation, TOC and COD analyses were performed before and after the photocatalytic reaction. The degradation intermediates and byproducts were identified using HRMS, providing mechanistic insights into the stepwise degradation of tetracycline. This sequential approach highlights the synergistic effect of adsorption and photocatalysis, where the initial preconcentration of tetracycline on the catalyst surface enhances the subsequent photocatalytic

degradation efficiency. The preliminary adsorption step increases the local concentration of tetracycline at the catalyst-solution interface, thereby facilitating more efficient charge transfer and reactive species attack during the photocatalytic process.

3. Results and discussion

3.1. Characterisations

3.1.1. XRD pattern. The X-ray diffraction (XRD) patterns of ZF, CQDs, and their composites (5ZQ, 10ZQ, and 15ZQ) confirm the efficient incorporation of CQDs into the ZIF-67 framework
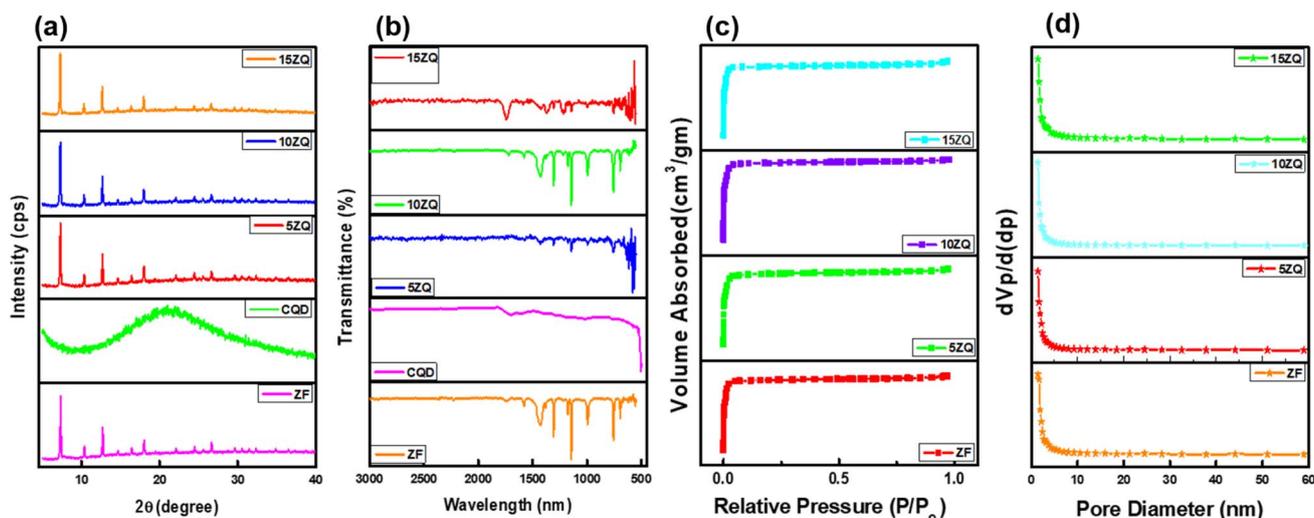

Fig. 1 (a) XRD profiles, (b) FT-IR spectra, (c) BET adsorption–desorption isotherms, and (d) BJH pore size distributions of ZF, CQDs, 5ZQ, 10ZQ, and 15ZQ.

Table 1 Summary of the BET surface area, average pore dimension, and cumulative pore capacity

Catalyst	BET surface area $(m^2\ g^{-1})$	Average pore dimension (nm)	Cumulative pore capacity $(cm^3\ g^{-1})$
ZF	1760	1.5908	0.6992
5ZQ	1540	1.5450	0.5965
10ZQ	1920	1.5119	0.7249
15ZQ	1600	1.5956	0.6383

with no detectable structural distortion (Fig. 1(a)). ZF displays a series of sharp and intense peaks at $2\theta \approx 7.3°$ (110), 10.4° (200), 12.7° (211), 14.8° (220), 16.4° (310), 18.0° (222), 24.6° (400), 26.7° (331), 29.6° (044), 32.4° (235), 34.6° (333), and 36.5° (315), consistent with the simulated and reported diffraction pattern of pristine ZIF-67. The broad amorphous hump observed at $2\theta \approx 22°$ in the CQD pattern corresponds to the (002) reflection of disordered sp²-hybridized carbon domains. The preservation of the characteristic ZF peaks in all composites indicates that CQD incorporation does not alter the crystal framework, while the slight variations in intensity suggest strong interfacial interaction between CQDs and ZF. This structural integrity, coupled with CQD-induced electronic synergy, is crucial for enhancing the material's adsorptive and photocatalytic performance.[12,27]

3.1.2. Fourier transform infrared (FTIR) analysis. The FTIR spectra of the parent materials (ZF and CQDs) and their composites (5ZQ, 10ZQ, and 15ZQ) confirm successful hybridization and the coexistence of multiple functional groups on the composite surface (Fig. 1(b)). The spectrum of pristine ZF exhibits distinct bands in the 990–670 cm^{-1} region, attributed to Co–N stretching vibrations of the imidazolate linkers,[28] along with characteristic peaks at $\sim1584\ cm^{-1}$ (C=N stretching of the imidazole ring), $\sim1410\ cm^{-1}$ and $\sim1350\ cm^{-1}$ (in-plane bending of the imidazole ring), and $\sim1147\ cm^{-1}$ (C–N stretching). In the CQD spectrum, the broad absorption band at

$\sim3430\ cm^{-1}$ corresponds to O–H stretching, while bands at $\sim1630\ cm^{-1}$ and $\sim1384\ cm^{-1}$ are associated with C=O stretching (or adsorbed water) and C–O vibrations, respectively.[27] Upon composite formation, the emergence of additional absorption bands near 1630 cm^{-1} and 1380 cm^{-1}, along with the slight shift and attenuation of Zn–N vibrations, indicates hydrogen bonding and electrostatic interactions between CQDs and the imidazolate framework. Furthermore, the gradual suppression of imidazolate ring peaks with increasing CQD content suggests surface modification and successful CQD embedding within the ZF lattice. These spectral changes corroborate the structural and optical variations observed in the complementary characterizations.

3.1.3. Nitrogen sorption and surface area analysis. The textural properties of CQDs, ZF, and their composites were assessed using N_2 adsorption–desorption isotherms and corresponding BJH pore size distribution plots (Fig. 1(c and d), respectively). The microporous nature of the materials was confirmed by the samples' quick uptake at low relative pressures ($P/P_0 < 0.1$) and plateau at higher pressures, which are characteristic of type I isotherms. The coexistence of micropores and small mesopores was indicated by the matching pore size distribution curves in Fig. 1(d), which display strong peaks in the 2–5 nm range. As presented in Table 1, the BET surface area and pore volume increased with CQD incorporation up to 10ZQ, suggesting that moderate CQD loading improved pore
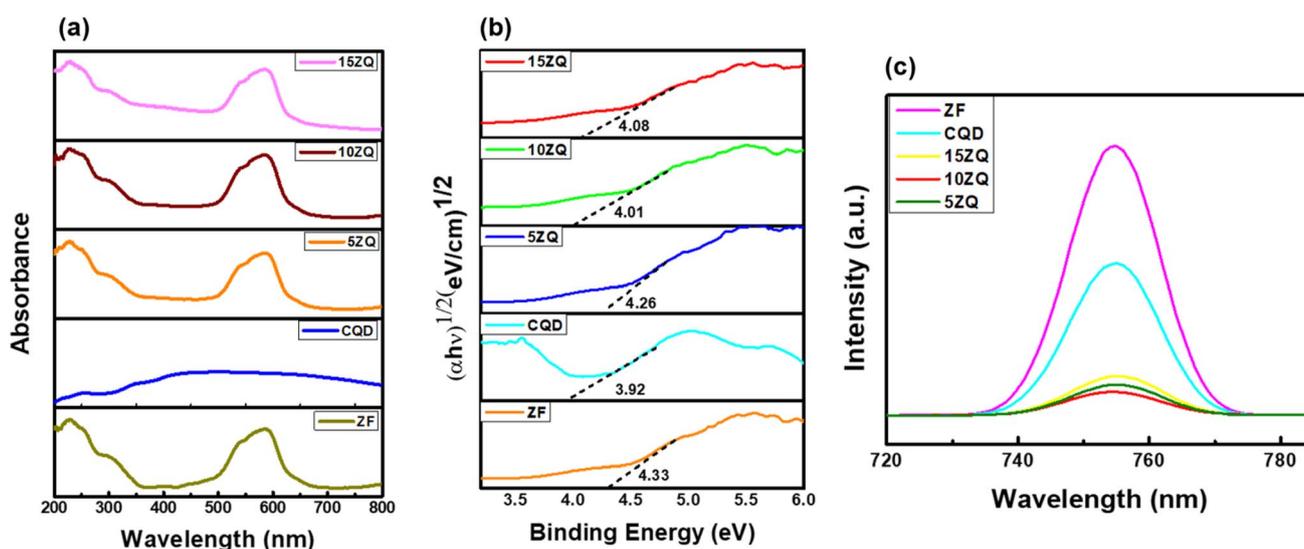

Fig. 2 (a) UV-vis DRS profiles, (b) Tauc plots, and (c) PL emission spectra of ZF, CQDs, 5ZQ, 10ZQ, and 15ZQ.

accessibility and structural stability. However, further addition (15ZQ) caused a decline in both parameters due to pore blockage and surface aggregation of excess CQDs. These findings demonstrate that 10ZQ exhibits the most favourable porosity and surface characteristics, which are beneficial for efficient adsorption and photocatalytic activity.

3.1.4. UV-visible diffuse reflectance (DRS) analysis. DRS analysis was conducted to assess the absorption features and band gap energies of ZF, CQDs, 5ZQ, 10ZQ, and 15ZQ. As illustrated in Fig. 2(a), all samples exhibited notable UV absorption. ZF displayed two prominent absorption peaks at 250–350 nm and 550–600 nm, attributed to the d–d transitions of Co^{2+} centers and π–π^* transitions of the imidazolate ligands, respectively. In contrast, CQDs showed a broad absorption band between 300 and 600 nm, corresponding to π–π^* and n–π^* transitions arising from sp^2-hybridized domains and surface functional groups, respectively.[29,30] Upon CQD incorporation, a progressive red shift and absorption edge broadening were observed in 5ZQ, 10ZQ, and 15ZQ, indicating enhanced light-harvesting capability and efficient electronic coupling between CQDs and the ZF framework.[28] The optical band gaps were derived from Tauc plots (Fig. 2(b)) using the following relation (eqn (2)):

$$(\alpha h\vartheta)^{0.5} = h\vartheta - E_g \qquad (2)$$

The optical band gaps were determined to be 3.94 eV (ZF), 3.92 eV (CQDs), 3.37 eV (5ZQ), 3.11 eV (10ZQ), and 3.21 eV (15ZQ).[31] The systematic band gap reduction from 3.94 eV in ZF to 3.11 eV in 10ZQ demonstrated the formation of intermediate electronic states and improved charge-transfer interactions upon CQD incorporation. The 10ZQ composite, exhibiting the lowest band gap (3.11 eV), signified superior light absorption and optical tunability, making it the most efficient among the synthesised samples for sunlight-driven photocatalytic applications.

3.1.5. Photoluminescence analysis. The recombination behaviour of photoinduced charge carriers in ZF, CQD, 5ZQ, 10ZQ, and 15ZQ was evaluated using photoluminescence (PL) spectroscopy.[32] All samples show an emission peak centered at approximately 750 nm, which is indicative of the radiative recombination of photogenerated electron-hole pairs, as seen in Fig. 2(c). The PL intensity directly reflects the recombination rate, where a higher intensity indicates more rapid recombination and thus reduced photocatalytic efficiency.[33] Among the samples, ZF shows the strongest PL emission, signifying significant charge carrier recombination. Upon the incorporation of CQDs, the PL intensity decreases notably due to the excellent electron-accepting and conductive ability of CQDs, which promotes charge separation. A further gradual decline in the PL intensity is observed for the composites in the order of ZF > 5ZQ > 15ZQ > 10ZQ, indicating progressively improved charge separation efficiency. The 10ZQ composite exhibits the lowest PL intensity, suggesting the marked decrease in electron-hole recombination and promotion of interfacial charge transport. In contrast, the slight increase in the PL intensity for 15ZQ implies that excessive CQD loading can cause aggregation,
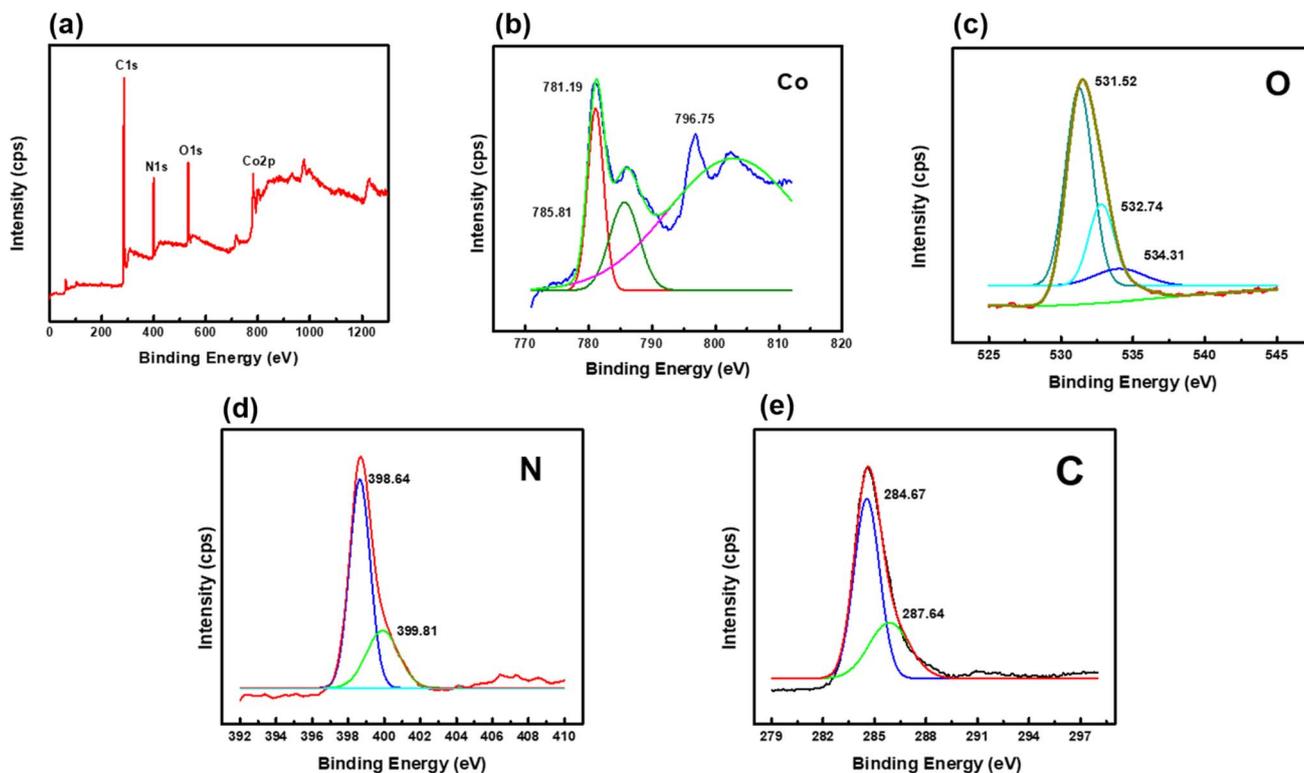

Fig. 3 XPS characterization of 10ZQ: (a) full survey scan and high-resolution spectra of (b) Co 2p, (c) O 1s, (d) N 1s, and (e) C 1s.

active site blocking, or light shielding, reducing the efficiency of photoexcited charge utilization. Thus, 10ZQ achieves the best balance between CQD dispersion, charge transfer, and light absorption, resulting in enhanced photocatalytic performance.

3.1.6. X-ray photoelectron spectroscopy (XPS) analysis. X-ray photoelectron spectroscopy (XPS) was used to determine the synthesized samples' elemental compositions, oxidation states, and core-level electronic environments. The survey spectrum of 10ZQ (Fig. 3(a)) validated the expected elemental framework by confirming the presence of Co, O, N, and C. A least-square Gaussian fitting model was used to deconvolute all spectra in order to identify the distinct chemical states. In the Co 2p spectrum (Fig. 3(b)), the two prominent peaks centered at 781.19 eV (Co $2p_{3/2}$) and 796.75 eV (Co $2p_{1/2}$) were assigned to Co(II) species, consistent with the typical spin–orbit splitting of cobalt in ZF.[34] Distinct shake-up satellite peaks in the range of 785.8–788.0 eV further confirmed the presence of high-spin Co^{2+} ions.[35] The O 1 s spectrum in Fig. 3(c) exhibited three deconvoluted peaks at 531.52 eV (C=O from carbonyl groups), 532.74 eV (C–O from hydroxyl, ether, or alcohol functionalities), and 535.0 eV (molecularly adsorbed O_2 or H_2O), demonstrating oxygen-containing surface species. The N 1s spectrum (Fig. 3(d)) displayed well-defined peaks corresponding to pyridinic N (398.7 eV), pyrrolic N (399.2 eV), and graphitic N (400.7 eV), confirming the presence of diverse nitrogen coordinations in the imidazolate linkers. Meanwhile, the high-resolution C 1s spectrum (Fig. 3(e)) exhibited a dominant peak at 284.67 eV, corresponding to sp^2/sp^3-hybridized C–C/C–H bonds, which

arise from both the imidazolate organic linker of ZIF-67 and the graphitic carbon framework of the CQDs. The additional component at 287.64 eV was attributed to O–C=O species associated with surface carbonyl and carboxyl functional groups, mainly originating from CQDs and confirming their successful incorporation into the ZIF-67 framework.[36,37] These observations collectively confirm the successful integration of CQDs within the ZF framework without altering the oxidation state of cobalt or the structural integrity of the imidazolate network, reinforcing the formation of the composite with rich surface functionality favorable for adsorption and photocatalysis.

3.1.7. FESEM surface and morphological analyses. The surface morphology and microstructural features of the fabricated samples were examined utilising FESEM, as illustrated in Fig. 4. The FESEM images (Fig. 4(a)) reveal that pristine ZF exhibits a well-defined dodecahedral morphology with uniformly distributed nanocrystals ranging between 300–500 nm. Such high crystallinity and structural uniformity are typical of hydrothermally synthesised ZIF-based frameworks and are crucial for enhancing the surface area and facilitating efficient adsorption and photocatalytic reactions. In Fig. 4(b), the FESEM image of CQDs shows no clearly distinguishable particles due to their extremely small size and quasi-spherical nature, which lie well below the resolution limit of FESEM. Despite their indistinct appearance, the successful formation of CQDs was confirmed through complementary techniques such as EDS and optical analyses. Upon CQD incorporation, the
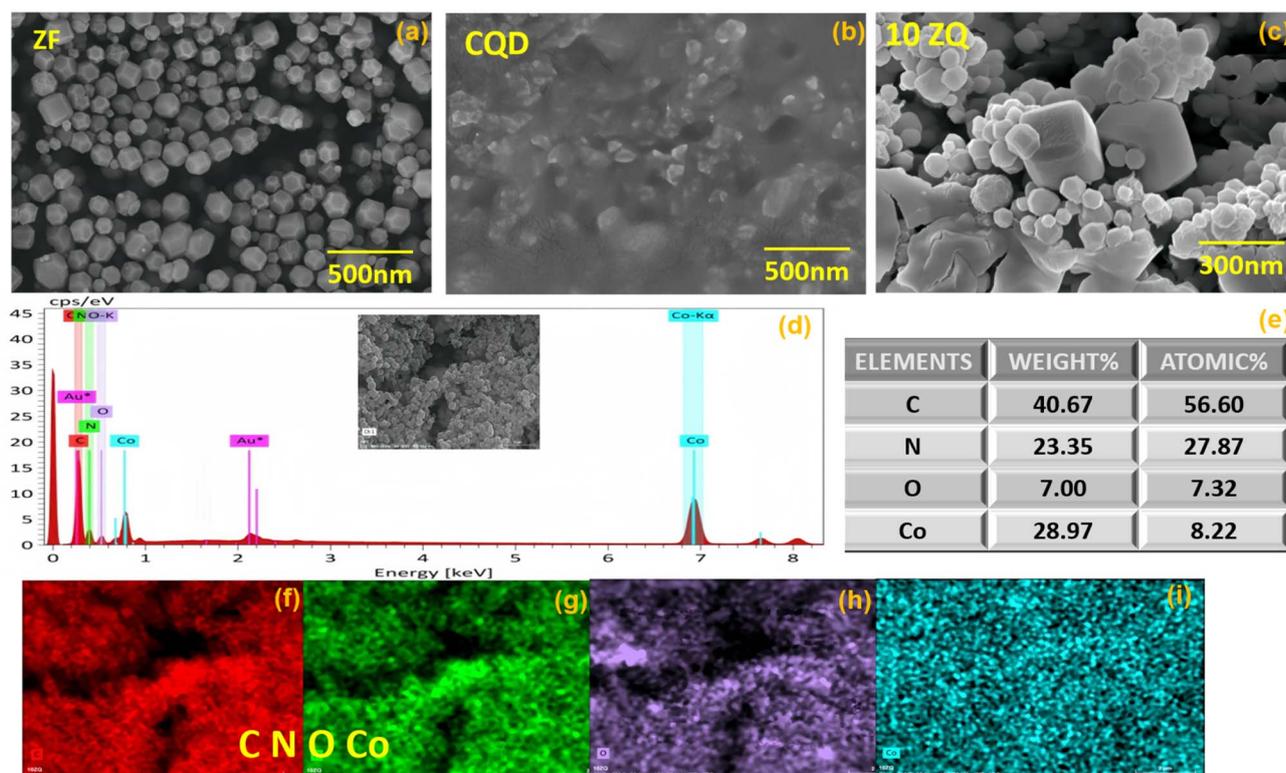

Fig. 4 FESEM micrographs of (a) ZF, (b) CQDs, and (c) the 10ZQ composite; (d and e) the corresponding EDS spectra; and (f–i) elemental mapping images of 10ZQ.

ELEMENTS	WEIGHT%	ATOMIC%
C	40.67	56.60
N	23.35	27.87
O	7.00	7.32
Co	28.97	8.22

characteristic ZF morphology is retained, confirming that the addition of CQDs does not disrupt the crystal framework. As shown in Fig. 4(c), the 10ZQ composite exhibits a slightly roughened surface and faint surface contrast variations, indicating the successful anchoring of CQDs onto the ZF surface, even though the individual CQDs cannot be distinctly resolved. The EDS spectrum (Fig. 4(d, e)) validates the elemental composition of the ZF/CQD composite, confirming the presence of C, N, Co, and O, which are the key constituents of the hybrid framework. Quantitative analysis indicates high atomic fractions of C (56.60%) and N (27.87%) from the 2-methylimidazole linker, with Co (8.22%) as the central metal ion, consistent with the reported ZF stoichiometry. The minor oxygen content is likely due to adsorbed surface species or partial oxidation during synthesis. Furthermore, elemental mapping (Fig. 4(f–i)) displays a consistent distribution of C, N, O, and Co across the entire microcrystal, confirming the homogeneous metal–ligand coordination and structural integrity of the synthesized ZF/CQD composite. These observations, coupled with EDS confirmation, strongly substantiate the successful integration of CQDs into the ZF framework without compromising its morphology or crystallinity.[38]

3.2. Effect of different light sources

Fig. 5(a) shows the results of a comprehensive investigation into the effects of visible light, UV light, and combined sunlight on the photocatalytic degradation efficiency of tetracycline. With degradation efficiencies of approximately 88% under visible light, 99% under UV light, and 97% under combined sunlight,

the catalyst demonstrates notable activity under all tested light conditions, according to the results. The higher energy of UV photons (wavelength < 400 nm) is responsible for the highest degradation rate under UV light. These photons have enough energy to directly excite electrons from the valence band to the conduction band, producing highly reactive species like superoxide anions ($^{\bullet}O_2^{-}$) and hydroxyl radicals ($^{\bullet}OH$). Significant activity is also exhibited by the catalyst under visible light, which is interesting because this suggests that it either has a narrow band gap or has been modified (by metal/nonmetal doping or heterojunction creation) to increase its absorption into the visible spectrum. The catalyst's practical relevance is also increased by its capacity to break down tetracycline by utilizing all the photons with lesser energy, which indicates that it is a good fit for solar-powered applications as well. Hence, we further studied the other parameters in sunlight.

3.3. Effect of the catalyst dose on tetracycline removal

The influence of the catalyst dosage on the tetracycline degradation efficiency was evaluated within the range of 0.05–0.30 g L^{-1} (Fig. 5(b)). Remarkably, 10ZQ exhibited >95% degradation efficiency across all tested dosages, demonstrating its superior photocatalytic performance. The highest degradation occurred at the lowest dosage (0.05 g L^{-1}), confirming the material's high intrinsic activity and efficient utilization of active sites. The slight decline in efficiency observed at intermediate dosages (0.15–0.20 g L^{-1}) can be attributed to the shielding effect because excessive catalyst loadings increase light scattering and turbidity, thereby reducing photon penetration. At higher
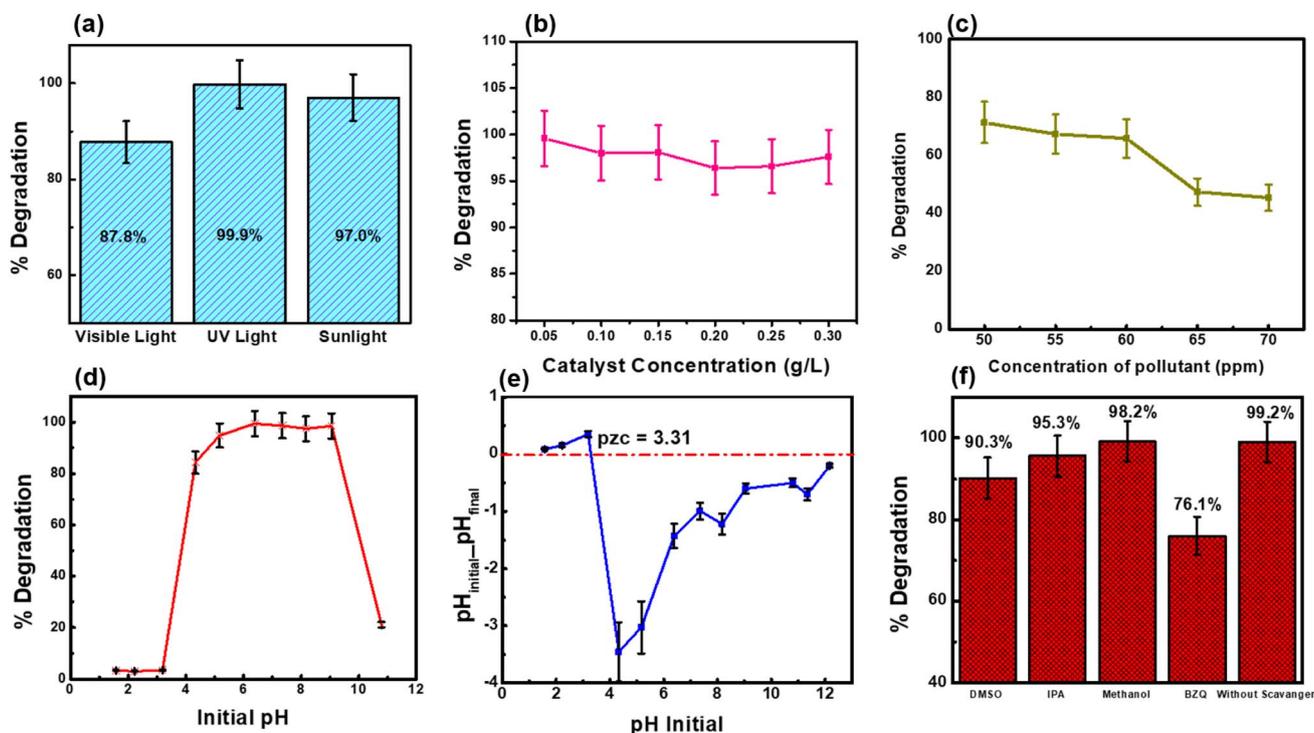

Fig. 5 Impact of (a) different light sources, (b) catalyst dose, (c) initial concentration, and (d) pH, (e) pzc studies, and (f) scavengers involved in the degradation of tetracycline.

dosages, particle agglomeration may further limit the accessible surface area and hinder active site exposure, resulting in a marginal reduction in degradation efficiency.

3.4. Dependence of tetracycline removal on the initial concentration

Fig. 5(c) depicts the dependence of the initial tetracycline concentration on the 10ZQ composite's removal effectiveness. When the initial tetracycline content was increased from 50 to 70 mg L^{-1}, the removal effectiveness of 10ZQ dropped from 75% to 45%. The restricted quantity of active sites on the photocatalyst's surface is the main cause of this decrease. At lower concentrations, tetracycline molecules readily occupy the accessible adsorption sites on 10ZQ, promoting efficient interaction with reactive species. However, as the concentration increases, these sites become saturated, leading to reduced adsorption and slower degradation. Excess tetracycline molecules at higher concentrations can also impede light penetration and diffusion toward active sites, restricting ROS generation and the overall photocatalytic activity. Furthermore, a concentration-driven shift in the adsorption–desorption equilibrium may favor desorption, causing previously adsorbed molecules to re-enter the solution. Consequently, site saturation, mass transfer resistance, and light shielding collectively contribute to the reduced tetracycline removal efficiency observed at elevated concentrations.

3.5. pH-dependent behaviour of tetracycline removal

The influence of pH on the photocatalytic degradation of tetracycline by 10ZQ was examined over a broad pH range (1–12) (Fig. 5(d)). The degradation efficiency is markedly low under strongly acidic conditions (pH < 3) but increases significantly between pH 3 and 5, reaching nearly 100% efficiency within the pH range of 6–9. Beyond pH 9, the photocatalytic performance gradually declines. The point of zero charge (pzc) of 10ZQ is determined to be 3.31 from the ΔpH ($pH_{initial}$–pH_{final}) plot (Fig. 5(e), inset). At pH < pzc, the catalyst surface is positively charged, while above the pzc, it is negatively charged. Since tetracycline exists in various protonation states with pKa values of 3.3, 7.7, 9.7, and 12, it predominantly exists as H_4TC, H_3TC, and H_2TC at pH 3.0, 7.0, and 9.0, respectively.[39] Under acidic conditions (pH < 3.3), both the catalyst surface and tetracycline molecules are protonated, leading to electrostatic repulsion and weak adsorption, which hinders degradation. Additionally, excess protons suppress the generation of reactive oxygen species (ROS), particularly 02D9OH, thus lowering photocatalytic efficiency. In the neutral to mildly basic range (pH 6–9), optimal degradation is achieved due to the favorable electrostatic attraction between the negatively charged 10ZQ surface and zwitterionic/deprotonated tetracycline molecules, ensuring efficient adsorption and charge transfer. Moreover, moderate alkalinity enhances 02D9OH generation, further improving degradation performance. However, at highly alkaline pH (>9), the efficiency decreases due to two main factors: (i) Excess OH^- ions act as scavengers, quenching active radicals like $^\bullet OH$ and $^\bullet O_2^-$ and (ii) both tetracycline and the 10ZQ surface become negatively charged, resulting in electrostatic repulsion and reduced adsorption. Additionally, ZF-based frameworks tend to agglomerate in acidic environments, leading to diminished photo-absorption and active site exposure. Conversely, at moderately basic pH, the negatively charged tetracycline molecules can effectively attract reactive groups (e.g., $^\bullet OH$) owing to their high electron density, enhancing photocatalytic degradation. Overall, the pH-dependent photocatalytic performance of 10ZQ is governed by the combined effect of surface charge modulation relative to the pH_{pzc}, which controls tetracycline adsorption through electrostatic interactions, and pH-regulated ROS generation efficiency, together determining the observed degradation behavior.

3.6. Identification of active reactive species via scavenger trapping experiments and the adsorption-degradation mechanism

Scavenger experiments were conducted under identical photocatalytic conditions to identify the dominant reactive oxygen species (ROS) involved in tetracycline degradation (Fig. 5(f)). The control experiment exhibited a high degradation efficiency of ~98–99%, confirming the excellent baseline photocatalytic activity of the system. The addition of hydroxyl radical ($^\bullet OH$) scavengers such as DMSO and IPA resulted in only a marginal decrease in the degradation efficiency (~96–98%), while methanol, which quenches both $^\bullet OH$ and photogenerated holes (h^+), caused negligible suppression.[40] These results indicate that $^\bullet OH$ radicals and direct hole oxidation play minor roles in the degradation process. In contrast, the degradation efficiency dropped significantly to ~76.1% upon the addition of benzoquinone (BQ), a selective scavenger for superoxide radicals ($^\bullet O_2^-$), clearly demonstrating that $^\bullet O_2^-$ is the principal oxidative species responsible for tetracycline degradation. This behavior suggests that photogenerated conduction band electrons are efficiently transferred to dissolved oxygen, leading to the formation of $^\bullet O_2^-$ radicals that drive the oxidative degradation pathways. Although photogenerated holes can react with water molecules or surface hydroxyl groups to generate $^\bullet OH$ radicals, their steady-state contribution remains minimal due to the extremely high reactivity and ultrashort lifetime of $^\bullet OH$, which promotes rapid recombination or an immediate reaction on the catalyst surface before accumulation in the bulk solution. Additionally, limited hole mobility further suppresses sustained $^\bullet OH$ formation. Consequently, $^\bullet O_2^-$, possessing a relatively longer lifetime and a higher diffusion capability, dominates the photocatalytic process and is more readily detected in scavenger experiments, while h^+ primarily plays an indirect role by initiating ROS formation rather than by acting as the main oxidative species.[41,42]

3.7. Effect of humic acid on photocatalytic performance

To evaluate the practical applicability of the photocatalyst under realistic water conditions, the influence of humic acid, a common natural organic matter present in surface waters, was investigated. Photocatalytic degradation experiments were carried out in the presence of humic acid concentrations
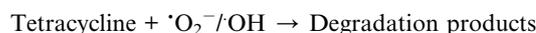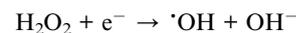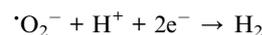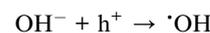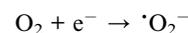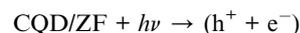
ranging from 1 to 5 mg L^{-1}. As shown in Fig. S1, the tetracycline removal efficiency gradually decreased from ~80% at 1 mg L^{-1} humic acid to ~64.8% at 5 mg L^{-1} humic acid. This behavior can be attributed to the competitive adsorption of humic acid and tetracycline on the active sites on the 10ZQ surface, which inhibits tetracycline degradation due to surface site occupation and partial scavenging of reactive species.[43] Despite these inhibitory effects, the catalyst maintained appreciable degradation efficiency even at higher humic acid concentrations, demonstrating its robustness and potential applicability in complex real-water matrices.

3.8. Proposed adsorption-photocatalytic degradation mechanism

The removal of tetracycline by the 10ZQ composite involves a synergistic adsorption–photocatalytic degradation mechanism, where adsorption serves as a crucial prestep enhancing the overall degradation efficiency. Tetracycline molecules engage in a variety of interactions with the surface of 10ZQ during the adsorption stage, such as hydrogen bonding, π–π interactions, van der Waals forces, pore filling, and electrostatic interactions.[5] While π–π stacking takes place between the conjugated structure of ZF/CQD and the aromatic rings of tetracycline, the presence of surface hydroxyl and carboxyl groups promotes hydrogen bonding with the polar functional groups of tetracycline. The porous framework of ZF provides abundant adsorption sites, and CQDs enhance surface functionality, aiding in the efficient capture and preconcentration of tetracycline molecules near active photocatalytic centers. Additionally, the surface charge of 10ZQ and the ionization state of tetracycline (depending on the pH) govern electrostatic attraction or repulsion, influencing the adsorption strength and efficiency. The band structure alignment of ZIF-67 and CQDs suggests the formation of a direct Z-scheme heterojunction. Upon light irradiation, the photocatalytic process initiates as

electron-hole pairs are generated at the CQD/ZF heterojunction. The CQDs act as an efficient electron mediator, facilitating charge separation and transfer. Based on these findings, the proposed mechanism begins with electron-hole separation in the CQD/ZF composite under light irradiation, followed by electron transfer from the core to the shell. The electron-rich catalyst surface interacts with O_2 to produce $\cdot O_2^-$, while holes oxidize hydroxyl ions to form $\cdot OH$ radicals. The generated $\cdot O_2^-$ and $\cdot OH$ species synergistically degrade tetracycline. The sequence of reactions involved can be expressed as: electron-hole separation in the CQD/ZF composite under light irradiation, followed by electron transfer from the core to the shell.

$$CQD/ZF + h\nu \rightarrow (h^+ + e^-)$$

$$O_2 + e^- \rightarrow \cdot O_2^-$$

$$H_2O \leftrightarrow H^+ + OH^-$$

$$OH^- + h^+ \rightarrow \cdot OH$$

$$\cdot O_2^- + H^+ + 2e^- \rightarrow H_2$$

$$H_2O_2 + e^- \rightarrow \cdot OH + OH^-$$

$$\text{Tetracycline} + \cdot O_2^-/\cdot OH \rightarrow \text{Degradation products}$$

When exposed to radiation in the presence of the synthesized photocatalyst, tetracycline molecules break into smaller compounds that may be completely converted to CO_2 and inorganic ions like sulfate, ammonium, and nitrate after prolonged exposure (Scheme 2).

3.9. Degradation pathway

The degradation mechanism of tetracycline during photocatalysis proceeds through a series of oxidative and bond-
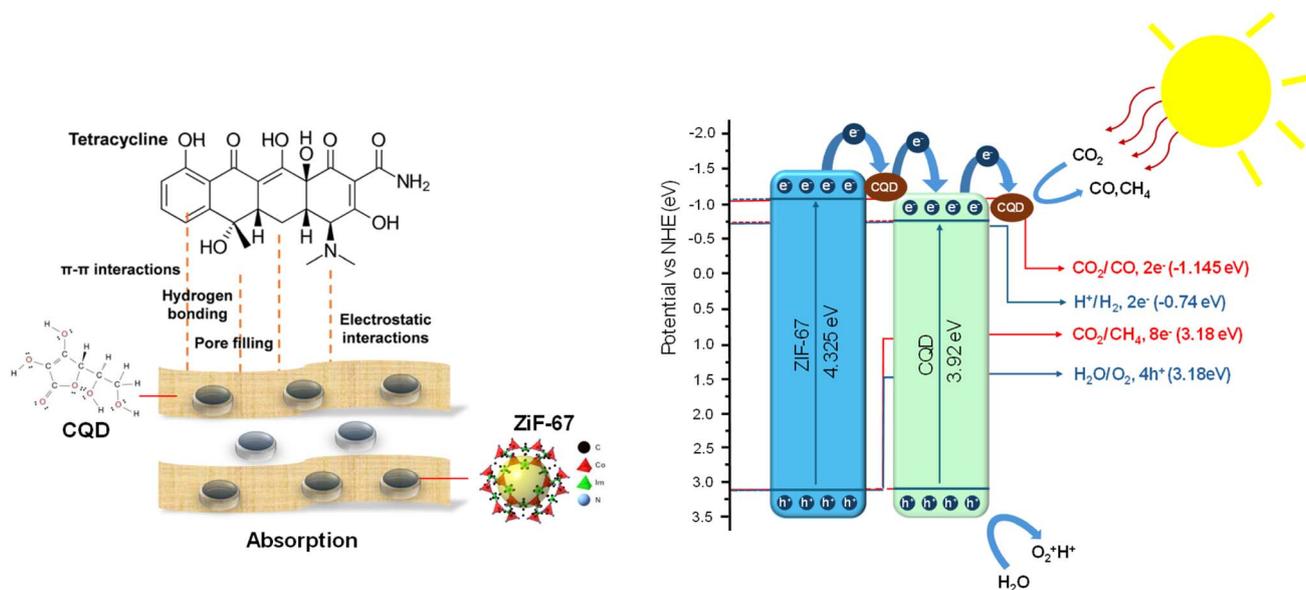
Scheme 2 Proposed adsorption–photocatalytic degradation mechanism of 10ZQ.

cleaving steps, resulting in the formation of lower-molecular-weight intermediates, as predicted using HRMS (Fig. S3) and illustrated in Scheme 3.[44,45] The initial tetracycline molecule, with a molecular ion peak at $m/z = 475$, undergoes N-demethylation and hydroxylation to form an intermediate at $m/z = 445$, indicating partial oxidation while retaining the tetracyclic core. This species undergoes further cleavage at the C–C and C–N bonds, leading to the generation of $m/z = 340$ and $m/z = 369$, where the former is characterized by the opening of ring structures and the removal of functional groups such as the dimethylamino side chain. The intermediate at $m/z = 369$ suggests a retained polyaromatic core with hydroxyl and amino functionalities. Continued degradation yields $m/z = 359$, indicative of deamination and hydroxylation processes, and $m/z = 276$, which corresponds to the partial cleavage of the tetracycline framework and the appearance of small aliphatic side chains. Successive oxidation steps lead to ring fragmentation, forming smaller intermediates such as $m/z = 175$, which presents a simplified aromatic ring bearing hydroxyl and ketone groups. The subsequent degradation leads to $m/z = 144$, $m/z = 141$, and $m/z = 125$, all representing mono- or dihydroxybenzoic acid-type structures, which are typical terminal aromatic intermediates in the degradation of polycyclic antibiotics. Finally, complete mineralization is suggested by the conversion of these benzenoid intermediates into simple products such as acetic acid and inorganic ions like CO_2, H_2O, NH_4^+, and NO_3^-, confirming that the pathway culminates in environmentally benign end-products. These observations are consistent with the reported pathways for the photocatalytic degradation of

tetracycline by advanced oxidation processes involving reactive oxygen species (ROS) like ˙OH and $O_2^{˙-}$.[39,46–49]

3.10. Adsorption isotherms

The SI contains the basic formulas and theoretical foundation for adsorption isotherms (S2). Adsorption isotherms are crucial for comprehending how adsorbates interact with the adsorbent's surface. Several isotherm models, including Langmuir, Freundlich, Halsey, Temkin, Harkins–Jura, and Dubinin–Radushkevich (D–R), were applied to the experimental data in order to examine the system's adsorption behavior (Fig. 6). Each model provides insights into the surface characteristics, adsorption mechanism, and adsorption capacity.[50,51] Among the tested models, the Langmuir isotherm achieved the best fit to the experimental data ($R^2 = 0.9909$), indicating that adsorption primarily occurs as a monolayer on a homogeneous adsorbent surface with finite identical sites. The maximum adsorption capacity ($q_m = 25.84$ mg g^{-1}) and positive Langmuir constant ($K_L = 0.0387$ L mg^{-1}) confirm favorable adsorption affinity. However, moderate fits with the Freundlich ($R^2 = 0.7602$), Halsey ($R^2 = 0.7602$), and Harkins–Jura ($R^2 = 0.7999$) models suggest that the surface exhibits some heterogeneity, with multilayer adsorption occurring on sites of varying energies, likely due to the pore structure and surface roughness. The Temkin isotherm ($R^2 = 0.7335$) further indicates that the heat of adsorption decreases linearly with surface coverage, reflecting adsorbate–adsorbent interactions and an endothermic adsorption process. The Dubinin–Radushkevich model resulted in a low mean adsorption energy ($E = 0.253$ kJ mol^{-1}), confirming
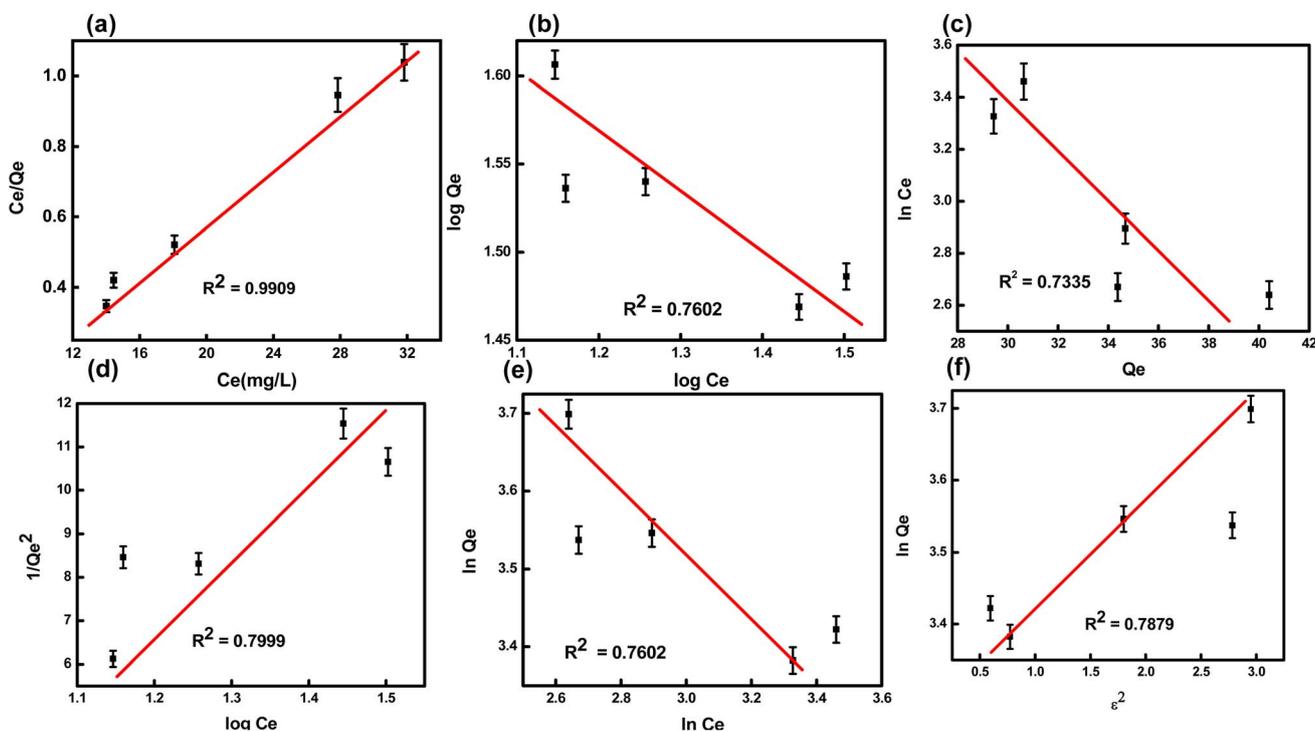

Fig. 6 Linear isotherm graphs corresponding to the (a) Langmuir, (b) Freundlich, (c) Dubinin–Radushkevich, (d) Harkins–Jura, (e) Temkin, and (f) Halsey models.
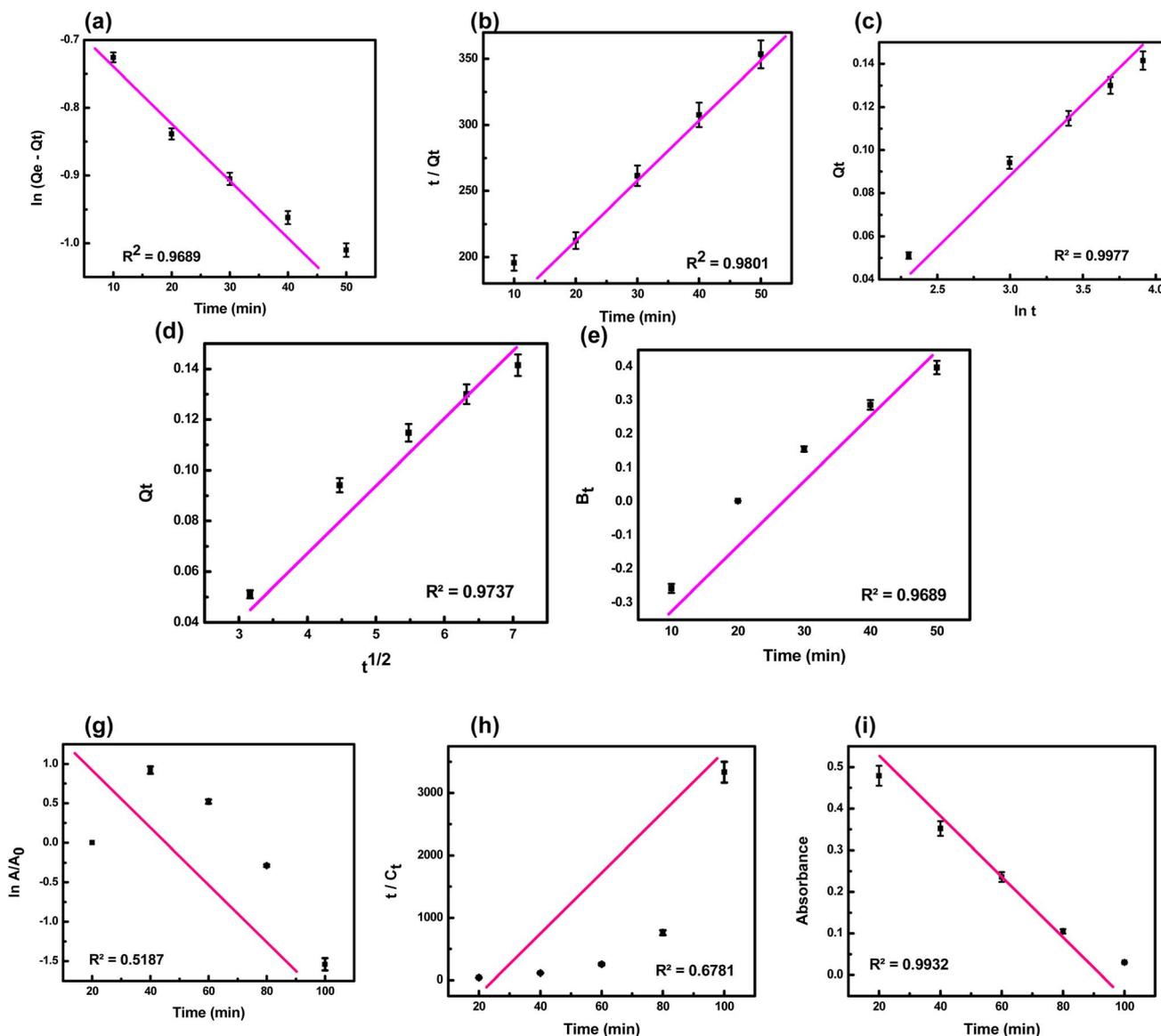
Fig. 7 Model-based linear fits of adsorption kinetics employing the (a) pseudo-first-order, (b) pseudo-second-order, (c) Elovich, (d) intraparticle diffusion, and (e) liquid-film diffusion models and the corresponding degradation kinetic profiles following (f) zero-order, (g) pseudo-first-order, (h) pseudo-second-order mechanisms, and (i) zero-order kinetics mechanisms.

that physisorption dominates the adsorption mechanism. Collectively, the results in Table 2 demonstrate that the adsorption process on the studied adsorbent is mainly physical in nature, with a predominant monolayer formation on a largely homogeneous surface, accompanied by multilayer adsorption phenomena on heterogeneous sites.[52]

3.11. Adsorption kinetics

The key equations and theoretical basis for adsorption kinetics are detailed in the SI S3. The adsorption kinetics of the studied system were analyzed using multiple kinetic models, namely, pseudo-first-order, pseudo-second-order, intraparticle diffusion, Elovich, and liquid film diffusion models.[53] The pseudo-first-order model exhibited poor correlation ($R^2 = 0.9689$,

Table 3) and a mismatch between experimental and calculated adsorption capacities, suggesting its unsuitability for describing the system. The pseudo-second-order model showed better agreement ($R^2 = 0.9801$), indicating chemisorption as a potential controlling mechanism.

However, the Elovich model provided the best fit with an exceptionally high correlation coefficient ($R^2 = 0.9977$), confirming that the adsorption process is strongly governed by chemisorption with an energetically uneven distribution of active sites. This highlights the progressive activation of sites during adsorption, making the Elovich model the most significant descriptor of the kinetic behavior.

Intraparticle diffusion analysis revealed a multilinear profile with a non-zero intercept, suggesting that diffusion into the pores contributes to the overall kinetics but is not the sole rate-

Table 2 Adsorption isotherm parameters for tetracycline adsorption on 10ZQ

Equilibrium isotherms	Equations	Parameters	Values
Langmuir	$\dfrac{C_e}{q_e} = \dfrac{1}{Q_m K_L} + \dfrac{1}{Q_m} C_e$	Q_m (mg g^{-1})	25.84
		K_L (L mg^{-1})	0.23
		R^2	0.9916
Freundlich	$q_e = K_F\, C_e^{1/n}$	K_F (mg g^{-1})	79.67
		$1/n$	0.2869
		R^2	0.7602
D–R	$\ln q_e = \ln Q_s - B\varepsilon^2$	Q_s (mg g^{-1})	5.73×10^{-12}
		B [(mol J^{-1})^2]	7.8411
		E (KJ mol^{-1})	0.253
		R^2	0.7879
Harkins–Jura	$\dfrac{1}{q^2e} = \left(\dfrac{B}{A}\right) - \dfrac{1}{A}\log C_e$	A	0.0858
		B	0.5286
		R^2	0.7999
Temkin	$q_e = B_T \ln K_T + B_T \ln C_e$	B_T (KJ mol^{-1})	32.94
		K_T (L mg^{-1})	6.45×10^{20}
		B (J mol^{-1})	0.0752
		R^2	0.7335
Halsey	$\ln q_e = \dfrac{1}{n}\ln K - \dfrac{1}{n}\ln C_e$	N	0.2869
		K (mg L^{-1})	4.19×10^{-6}
		R^2	0.7602

limiting step, while the liquid film diffusion model (Fig. 7) confirmed that boundary layer resistance also influences the adsorption process. Taken together, these findings indicate that the adsorption mechanism is a complex process dominated by chemisorption (Elovich model), with contributions from diffusion mechanisms that control the rate at different stages.[54,55]

3.12. Photocatalytic degradation kinetics

The antibiotic's photocatalytic degradation kinetics were evaluated by monitoring its concentration using UV-vis spectrophotometry, providing degradation rates and reaction times. Basic formulae are explained in the SI S4. The degradation kinetics were examined using zero-order, pseudo-first-order, and pseudo-second-order models.[56,57] Among these, the zero-order model provided the best fit ($R^2 = 0.9932$) and a rate constant of $k = 0.0057$ min^{-1}, showing a nearly perfect linear decrease in concentration with time. This indicates that the degradation proceeds at a constant rate, independent of the remaining concentration. While the adsorption of tetracycline on the photocatalyst follows Elovich kinetics, indicative of chemisorption, the photocatalytic degradation under illumination exhibits zero-order kinetics. This occurs because adsorption rapidly saturates the catalyst surface, and under steady light irradiation, the generation of reactive species ($\bullet O_2^-$ and h$^+$) remains constant. Therefore, the degradation rate becomes independent of the tetracycline concentration, with photocatalysis controlling the overall reaction rate. In the combined process, chemisorption facilitates substrate access to active sites, but the light-driven reactions dominate the kinetics. The efficiency of various photocatalysts, including CQDs, ZF, 5ZQ, 10ZQ, and 15ZQ, was compared in a series of the same experiments. The results revealed that 10ZQ outperformed the others, exhibiting a rate constant of 0.0057, which is significantly higher than that of other composites, 5ZQ (0.0033 min^{-1}) and 15ZQ (0.0038 min^{-1}) (Fig. S2). To evaluate the improved performance of the composite materials, a synergy factor (R) was computed using eqn (3):[57]

$$R = \frac{k_{\text{CQDs+ZF}}}{k_{\text{CQDs}} + k_{\text{ZF}}} \qquad (3)$$

The photodegradation rate constants of the CQD/ZF composites and their constituent parts were used to calculate this factor. 10ZQ had the highest synergy factor of 0.239, which was connected with its higher photocatalytic degradation efficiency, compared to 0.138 for 5ZQ and 0.159 for 15ZQ. The enhanced photocatalytic activity of CQD/ZF composites for TC degradation can be attributed to the synergistic interactions between the two components, which together overcome the limitations of individual photocatalysts. The intimate interface between CQDs and ZIF-67 facilitates rapid charge transfer and enhances the heterojunction effect, leading to the efficient formation of reactive oxygen species (ROS) such as superoxide radicals ($^{\bullet}O_2^-$) and hydroxyl radicals ($^{\bullet}OH$), which are primarily responsible for breaking down the complex tetracycline molecules. The synergistic effect is highly dependent on the optimal loading ratio, and the 10ZQ composite provides the maximum balance between light absorption, surface active sites, and charge transfer pathways, resulting in the highest synergy factor and superior photocatalytic degradation efficiency compared to higher or lower loadings, which may lead to aggregation or blockage of active sites.

3.13. Mineralisation studies

To assess the degree of tetracycline mineralization and verify degradation beyond mere transformation, TOC and COD measurements were conducted under optimized photocatalytic conditions using the 10ZQ composite (Fig. 8(a)). After 60 min of irradiation, approximately 76% TOC removal and 78% COD reduction were achieved, indicating the substantial oxidation of
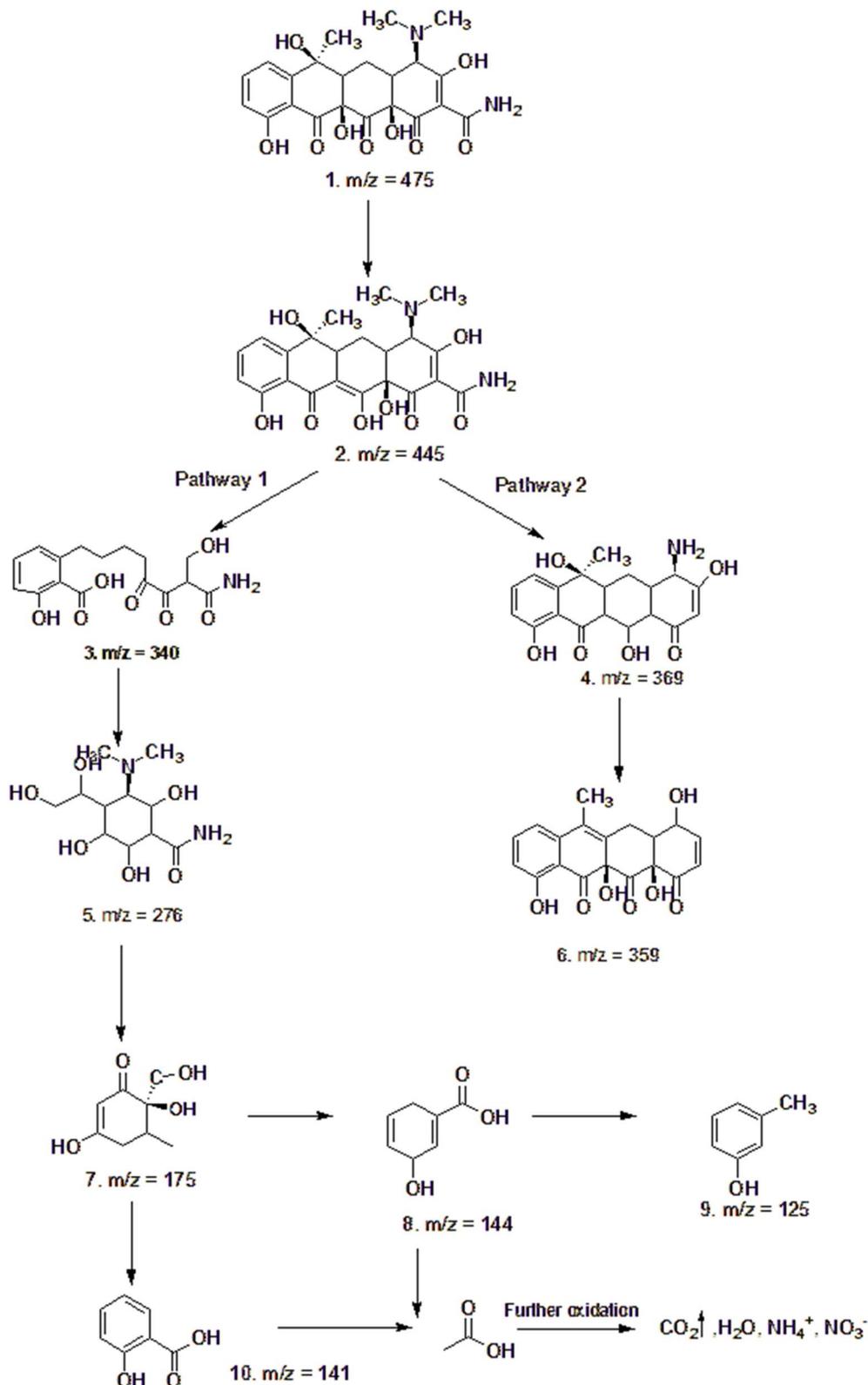
Scheme 3 Potential photocatalytic reaction route of tetracycline.

tetracycline and its intermediates into CO_2, H_2O, and simpler inorganic species. The slightly higher COD removal than TOC removal suggests the generation of short-chain oxygenated intermediates during the degradation process, which are eventually oxidized under prolonged irradiation. This observation correlates with the HRMS analysis, which confirmed the

Table 3 Adsorption and degradation kinetic parameters

Kinetic models	Equations	Parameters	Values
Adsorption kinetics			
Pseudo-first-order	$-\ln\left(1 - \dfrac{q_t}{q_e}\right) = k_1 t$	K_1 (min^{-1})	0.01589
		Q_e (mg g^{-1})	0.208
		R^2	0.9689
Pseudo-second-order	$\dfrac{t}{q_t} = \dfrac{1}{k^2 q e^2} + \dfrac{t}{q_e}$	K_2 (min^{-1})	0.243
		Q_e (mg g^{-1})	0.118
		R^2	0.9801
Intraparticle diffusion	$q_t = k_1 t^{1/2} + C_1$	K_1 (min^{-1})	0.0228
		C_1 (mg g^{-1})	0.0146
		R^2	0.9737
Elovich	$q_t = {}^1\!\big/\beta \ln(\alpha\beta) + {}^1\!\big/\beta \ln(t)$	A (mg g^{-1} min^{-1})	0.01435
		b (g mg^{-1})	17.880
		R^2	0.9977
Liquid-film	$-\ln(1 - F) = K_{fd} \times t$	K_{fd}	0.0159
		R^2	0.9689
Degradation kinetics			
Zero-order	$C_t = C_o - K_t$	K_t (min^{-1})	0.0057
		R^2	0.9932
Pseudo-first-order	$\ln(C_t) = \ln(Co) - k_1 t$	K_1 (min^{-1})	0.0215
		R^2	0.5187
Pseudo-second-order	$\dfrac{t}{C_t} = \dfrac{1}{k_2 C_o^2} + \dfrac{t}{C_o}$	K_2 (min^{-1})	1.028
		R^2	0.6781

progressive fragmentation of aromatic rings and degradation of the molecular structure. The close agreement between TOC and COD removal further demonstrates that the degradation process is not merely a surface reaction but leads to near-complete mineralization. These results reaffirm the high oxidative potential, structural stability, and reusability of the 10ZQ photocatalyst, making it a promising candidate for sustainable water purification and antibiotic-contaminated wastewater treatment applications.

3.14. Reusability studies

Determining a nanocomposite's durability for practical usage is as important as evaluating how well it adsorbs pollutants. The stability and consistency of the 10ZQ nanocomposite were
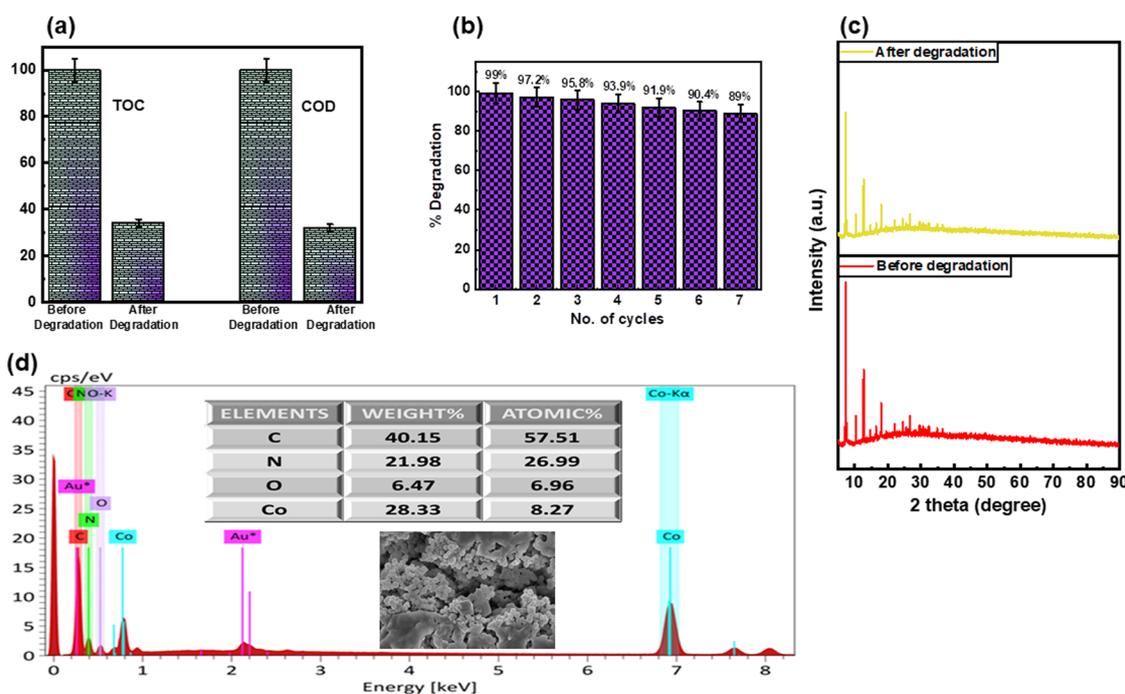

Fig. 8 (a) TOC/COD analysis, (b) reusability cycles, (c) XRD spectra of 10ZQ before and after use, and (d) FESEM image and EDS analysis of 10ZQ after use.

Table 4 Comparison of the TC degradation efficiency of 10ZQ and other reported catalysts

Catalyst	Concentration of tetracycline (mg L^{-1})	Dose of the catalyst (g L^{-1})	Degradation efficiency (%)	Time (min)	References
MoS_2/TiO_2	10	25	95	100	58
Nano-TiO_2/micro-ZnO	20	2.5	78.94	165	59
$MoO_3/Ag/C_3N_4$	20	0.02	89	100	60
CuBTC/g-C_3N_4	25	0.1	97.4	60	57
AgBr/$CuBi_2O_4$	10	0.5	90	60	61
Bi_2O_3/Sb_2S_3	10	0.03	91.5	120	62
NZVI/g-C_3N_4@EGC	30	0.03	98.5	30	63
CQD/ZiF-67	50	0.05	99	60	This work

examined using a series of recycling tests. The goal was to analyze how it functions across several reaction cycles under the same experimental conditions. After each cycle and before use in the next cycle, the catalyst underwent centrifugation, washing, and drying. As shown by the results in Fig. 8(b), even after seven cycles, the efficacy of the catalyst stayed at 89%. Due to the unavoidable loss of some catalyst during retrieval, the removal efficacy dropped from 99% to 89%. This implies that 10ZQ can be efficiently recycled as a catalyst.

Additionally, untreated intermediates have the ability to adhere to the catalyst surface, obstructing active sites and reducing efficiency. The post use XRD pattern of 10ZQ (Fig. 8(c)) closely matched that of the fresh sample, with no new peaks or noticeable shifts, confirming its excellent structural stability after seven adsorption–photodegradation cycles. The retained sharp reflections indicated that the crystalline framework remained intact and resistant to photocorrosion or leaching. Additionally, the structural and compositional stability of the reused 10ZQ nanocomposite was further confirmed by FESEM and EDS analyses after repeated adsorption–photocatalytic cycles. As shown in Fig. 8(d), the post-cycling FESEM images revealed that the morphology of 10ZQ remained largely unchanged compared to the fresh sample, with no signs of particle agglomeration, surface collapse, or phase transformation. The corresponding EDS spectra and elemental mapping of the reused catalyst confirmed the uniform distribution of the constituent elements, with no detectable loss of metal species, indicating the absence of significant leaching during repeated use. These observations, together with the post use XRD results, clearly demonstrate the excellent structural integrity, compositional stability, and recyclability of the 10ZQ nanocomposite during successive adsorption–photocatalytic cycles.

3.15. Comparison with the literature

The developed 10ZQ composite's superior performance, in terms of its tetracycline removal efficiency, is highlighted by a comparative analysis (Table 4) with previously reported photocatalysts, indicating its prospects as a highly efficient and sustainable photocatalyst for environmental remediation.

4. Conclusion

In summary, a series of CQD-modified ZIF-67 (ZF) composites with different CQD loadings (5ZQ, 10ZQ, and 15ZQ) was

successfully synthesised *via* a simple hydrothermal approach and evaluated for the adsorptive and photocatalytic removal of tetracycline. Structural analyses (XRD, FTIR, and XPS) confirmed the successful incorporation of CQDs into the ZF framework without compromising its crystallinity, while optical studies revealed a significant band gap reduction and enhanced visible-light absorption. Morphological characterization demonstrated the uniform distribution and intimate interfacial contact between ZF and CQDs, which facilitated efficient charge separation, as supported by PL results. The integrated adsorption–photocatalysis experiments revealed that the composite materials effectively removed tetracycline, with 10ZQ exhibiting the highest performance (~99% degradation within 60 min) due to its optimal CQD loading, which promoted strong light absorption and suppressed electron-hole recombination. Among the six adsorption isotherm models tested, the Langmuir model best described the adsorption behaviour, indicating monolayer adsorption on a homogeneous surface. Kinetic analyses using five models revealed that the Elovich model provided the best fit, indicating that chemisorption was the rate-controlling step. Furthermore, degradation kinetics followed a zero-order reaction model, highlighting the steady-state nature of the photocatalytic process under optimised conditions. Radical scavenging tests revealed that superoxide radicals ($^{\bullet}O_2^-$) served as the primary reactive species driving the degradation mechanism. The photocatalyst retained significant activity in the presence of humic acid, highlighting its potential for application in realistic wastewater systems containing natural organic matter. The catalyst also showed remarkable stability and reusability over multiple cycles, underscoring its potential for practical water treatment. Additionally, TOC and COD analyses exhibited 76% and 78% removal, respectively, validating the near-complete mineralisation of TC into CO_2 and H_2O, in accordance with HRMS analysis, which gives the degradation pathway. Overall, this study demonstrates that coupling ZF with CQDs creates a synergistic heterojunction system with superior adsorption capacity, enhanced charge carrier dynamics, and excellent photocatalytic efficiency. While the present study demonstrates promising photocatalytic performance, aspects such as long-term catalyst stability, the influence of complex real-water matrices, and scale-up feasibility were not fully explored and will be addressed in future work. Nevertheless, the results highlight the strong potential of the CQD-MOF composite strategy for efficient and sustainable

remediation of antibiotic-contaminated wastewater under solar-light conditions.

Author contributions

Khizra Ali: designed and performed the experiments, analysed data and co-wrote the paper. Palkaran Sethi: supervised the research, designed experiments and co-wrote the paper. Soumen Basu: supervised, the research and co-wrote the paper.

Conflicts of interest

The authors declare that there are no conflicts of interest, financial or personal, that could have influenced the research presented in this paper.

Data availability

The data supporting the findings of this study, including characterization results, adsorption and degradation kinetics, and isotherm studies, are presented within the article and the details of characterization methods used, detailed adsorption isotherms and adsorption and photocatalytic degradation kinetics equations and theories with HRMS plot in the accompanying supplementary information (SI) file. Supplementary information is available. See DOI: https://doi.org/10.1039/d5su00898k.

Acknowledgements

References

1 S. Singh, N. Sivaram, D. S. Dhanjal, H. Assefa, J. Singh and P. C. Ramamurthy, Navigating the Complexity of Emerging Contaminants: Sources, Impacts, and Remediation Strategies, *J. Indian Inst. Sci.*, 2024, **104**(2), 519–553, DOI: 10.1007/s41745-024-00446-4.

2 J. Muhammad, S. Khan, J. Q. Su, A. E.-L. Hesham, A. Ditta, J. Nawab and A. Ali, Antibiotics in Poultry Manure and Their Associated Health Issues: A Systematic Review, *J. Soils Sediments*, 2020, **20**(1), 486–497, DOI: 10.1007/s11368-019-02360-0.

3 N. Morin-Crini, E. Lichtfouse, G. Liu, V. Balaram, A. R. L. Ribeiro, Z. Lu, F. Stock, E. Carmona, M. R. Teixeira, L. A. Picos-Corrales, J. C. Moreno-Piraján, L. Giraldo, C. Li, A. Pandey, D. Hocquet, G. Torri and G. Crini, Worldwide Cases of Water Pollution by Emerging Contaminants: A Review, *Environ. Chem. Lett.*, 2022, **20**(4), 2311–2338, DOI: 10.1007/s10311-022-01447-4.

4 P. Sangeetha and S. Jagtap, Impact of Novel Remediation Technology: Significant Role in the Removal of Toxic Pollutants via Sustainable Approaches, in *Industrial Microbiology and Biotechnology: an Insight into Current Trends*, ed. P. Verma, Springer Nature Singapore, Singapore, 2024, pp. 679–701, DOI: 10.1007/978-981-97-1912-9_27.

5 B. Garg, P. Sethi and S. Basu, Strategic Innovation in CuBTC/PANI Nanocomposites for Dye Remediation: A Holistic Approach for Enhancing Adsorption, Isotherms, and Kinetic Studies, *RSC Sustain.*, 2025, **3**, 2311–2324, DOI: 10.1039/d5su00056d.

6 S. Shao and X. Wu, Microbial Degradation of Tetracycline in the Aquatic Environment: A Review, *Crit. Rev. Biotechnol.*, 2020, **40**(7), 1010–1018, DOI: 10.1080/07388551.2020.1805585.

7 A. Singh, S. G. Pratap and A. Raj, Occurrence and Dissemination of Antibiotics and Antibiotic Resistance in Aquatic Environment and Its Ecological Implications: A Review, *Environ. Sci. Pollut. Res.*, 2024, **31**(35), 47505–47529, DOI: 10.1007/s11356-024-34355-x.

8 R. Daghrir and P. Drogui, Tetracycline Antibiotics in the Environment: A Review, *Environ. Chem. Lett.*, 2013, **11**(3), 209–227, DOI: 10.1007/s10311-013-0404-8.

9 C. V. Gómez-Pacheco, M. Sánchez-Polo, J. Rivera-Utrilla and J. López-Peñalver, Tetracycline Removal from Waters by Integrated Technologies Based on Ozonation and Biodegradation, *Chem. Eng. J.*, 2011, **178**, 115–121, DOI: 10.1016/j.cej.2011.10.023.

10 L. Reggiane and L. Féris, Use of Functinalized Adsorbents for Tetracycline Removal in Wastewater: Adsorption Mechanism and Comparison with Activated Carbon, *J. Environ. Sci. Health, Part A: Toxic/Hazard. Subst. Environ. Eng.*, 2020, **55**, 1–11, DOI: 10.1080/10934529.2020.1827654.

11 P. Sethi, S. Barman and S. Basu, CuBTC–Clay Composites with Tunable Ratios for Antibiotic Removal: Unraveling Isotherm, Kinetic, and Thermodynamic Study, *Mater. Adv.*, 2025, **6**, 6370–6385, DOI: 10.1039/D5MA00639B.

12 H. Bansal, P. Sethi and S. Basu, Nanoflower-like ZnO-Carbon Quantum Dot Heterostructures for Solar-Driven Degradation of Methylene Blue: A High-Performance and Recyclable Photocatalyst for Sustainable Wastewater Treatment, *Mater. Adv.*, 2025, **6**, 7585–7598, DOI: 10.1039/d5ma00804b.

13 S. Li, X. Li, Y. Liu, P. Zhang, J. Zhang and B. Zhang, Interfacial Engineering of a Plasmonic Ag/Ag2CO3/C3N5 S-Scheme Heterojunction for High-Performance Photocatalytic Degradation of Antibiotics, *Chin. J. Catal.*, 2025, **72**, 130–142, DOI: 10.1016/S1872-2067(25)64652-3.

14 S. Li, X. Wang, B. Xue, D. Feng, Y. Liu and W. Jiang, Flower-like Ag/Ag2O/Bi12O17Cl2 Heterojunction for Photocatalytic Removal of Antibiotics: Synergetic Effect of Plasmonic Effect and p–n Heterojunction, *J. Mater. Sci. Technol.*, 2026, **246**, 237–246, DOI: 10.1016/j.jmst.2024.12.088.

15 S. Natarajan, H. C. Bajaj and R. J. Tayade, Recent Advances Based on the Synergetic Effect of Adsorption for Removal of Dyes from Waste Water Using Photocatalytic Process, *J. Environ. Sci.*, 2018, **65**, 201–222, DOI: 10.1016/j.jes.2017.03.011.

16 P. Sethi, S. Barman and S. Basu, Eco-Friendly Tetracycline Remediation Using Robust and Highly Reusable ZIF-67/g-C3N4 Nanocomposites with Coupled Adsorption and Photocatalytic Pathways: A Deep Dive into Isotherms, Kinetics, Thermodynamics, and Degradation Pathways, *ACS Sustainable Resour. Manage.*, 2025, **3**, 244–259, DOI: 10.1021/acssusresmgt.5c00536.

17 A. Khadir, M. Motamedi, M. Negarestani, M. Sillanpää and M. Sasani, Preparation of a Nano Bio-Composite Based on Cellulosic Biomass and Conducting Polymeric Nanoparticles for Ibuprofen Removal: Kinetics, Isotherms, and Energy Site Distribution, *Int. J. Biol. Macromol.*, 2020, **162**, 663–677, DOI: 10.1016/j.ijbiomac.2020.06.095.

18 A. Rathi, S. Basu and S. Barman, Adsorptive Removal of Fipronil from Its Aqueous Solution by Modified Zeolite HZSM-5: Equilibrium, Kinetic and Thermodynamic Study, *J. Mol. Liq.*, 2019, **283**, 867–878, DOI: 10.1016/j.molliq.2019.02.140.

19 Y. Wang, Z. Lan, X. Huang, H. Liu and J. Guo, Study on Catalytic Effect and Mechanism of MOF (MOF = ZIF-8, ZIF-67, MOF-74) on Hydrogen Storage Properties of Magnesium, *Int. J. Hydrogen Energy*, 2019, **44**(54), 28863–28873, DOI: 10.1016/j.ijhydene.2019.09.110.

20 S. Roy, J. Darabdhara and M. Ahmaruzzaman, ZnO-Based Cu Metal–Organic Framework (MOF) Nanocomposite for Boosting and Tuning the Photocatalytic Degradation Performance, *Environ. Sci. Pollut. Res.*, 2023, **30**(42), 95673–95691, DOI: 10.1007/s11356-023-29105-4.

21 C. Yang, X. You, J. Cheng, H. Zheng and Y. Chen, A Novel Visible-Light-Driven In-Based MOF/Graphene Oxide Composite Photocatalyst with Enhanced Photocatalytic Activity toward the Degradation of Amoxicillin, *Appl. Catal., B*, 2017, **200**, 673–680, DOI: 10.1016/j.apcatb.2016.07.057.

22 S. J. Phang and L. L. Tan, Recent Advances in Carbon Quantum Dot (CQD)-Based Two Dimensional Materials for Photocatalytic Applications, *Catal. Sci. Technol.*, 2019, **9**(21), 5882–5905, DOI: 10.1039/c9cy01452g.

23 R. Ghasemzadeh and K. Akhbari, Degradation of Acid Blue 41 with Carbon Quantum Dots@MOF-808 Nanocomposite as a Biocompatible Photocatalyst under Visible Light, *J. Photochem. Photobiol., A*, 2025, **458**, 115984, DOI: 10.1016/j.jphotochem.2024.115984.

24 Z. Song, C. Xing, Y. Yuan, B. Liu, X. Zhang, J. Liu, Y. Huang, D. Han and J. Zhang, The Bi-MOF@CQDs@g-C3N4 Heterojunction Photocatalyst Enhances Interface Charge Transfer via Electron Bridges to Promote Rapid Norfloxacin Degradation, *Sep. Purif. Technol.*, 2026, **380**, 135296, DOI: 10.1016/j.seppur.2025.135296.

25 J. Qian, F. Sun and L. Qin, Hydrothermal synthesis of zeolitic imidazolate framework-67 (ZIF-67) nanocrystals, *Mat. Lett.*, 2012, **82**, 220–223.

26 X. Guo, T. Xing, Y. Lou and J. Chen, Controlling ZIF-67 Crystals Formation through Various Cobalt Sources in Aqueous Solution, *J. Solid State Chem.*, 2016, **235**, 107–112, DOI: 10.1016/j.jssc.2015.12.021.

27 E. S. Elmorsy, W. A. Amer, A. Mahrous and M. M. Ayad, Insight into the Novel ZIF-8@N-CQDs/ZIF-67 Nanocomposite for Photocatalytic Degradation of Methylene Blue under Visible Light Irradiation, *Mater. Sci. Eng. B*, 2023, **298**, 116900, DOI: 10.1016/j.mseb.2023.116900.

28 Y. Meng, L. Zhang, H. Jiu, Q. Zhang, H. Zhang, W. Ren, Y. Sun and D. Li, Construction of G-C3N4/ZIF-67 Photocatalyst with Enhanced Photocatalytic CO2 Reduction Activity, *Mater. Sci. Semicond. Process.*, 2019, **95**, 35–41, DOI: 10.1016/j.mssp.2019.02.010.

29 Z. Huang, J. Zhou, Y. Zhao, H. Cheng, G. Lu, A. W. Morawski and Y. Yu, Stable Core–Shell ZIF-8@ZIF-67 MOFs Photocatalyst for Highly Efficient Degradation of Organic Pollutant and Hydrogen Evolution, *J. Mater. Res.*, 2021, **36**(3), 602–614, DOI: 10.1557/s43578-021-00117-5.

30 K. Akbar, E. Moretti and A. Vomiero, Carbon Dots for Photocatalytic Degradation of Aqueous Pollutants: Recent Advancements, *Adv. Opt. Mater.*, 2021, **9**(17), 2100532, DOI: 10.1002/adom.202100532.

31 Q. Chen, S. Li, H. Xu, G. Wang, Y. Qu, P. Zhu and D. Wang, Co-MOF as an Electron Donor for Promoting Visible-Light Photoactivities of g-C3N4 Nanosheets for CO2 Reduction, *Chin. J. Catal.*, 2020, **41**(3), 514–523, DOI: 10.1016/S1872-2067(19)63497-2.

32 A. Ekinci, S. Kutluay, Ö. Şahin and O. Baytar, Green Synthesis of Copper Oxide and Manganese Oxide Nanoparticles from Watermelon Seed Shell Extract for Enhanced Photocatalytic Reduction of Methylene Blue, *Int. J. Phytoremediation*, 2023, **25**(6), 789–798, DOI: 10.1080/15226514.2022.2109588.

33 S. Norouzi, A. Esmaeili, K. Dashtian, R. Zare-Dorabei, M. Mahdavi, M. Noroozifar and K. Kerman, Carbon Dot-ZIF-67-Infused Tragacanth Hydrogel Films: Leveraging Tunable Luminescence through Displacement Mechanisms for Anthrax Detection, *Microchim. Acta*, 2025, **192**(2), 121, DOI: 10.1007/s00604-025-06984-7.

34 D. Barreca, C. Massignan, S. Daolio, M. Fabrizio, C. Piccirillo, L. Armelao and E. Tondello, Composition and Microstructure of Cobalt Oxide Thin Films Obtained from a Novel Cobalt(II) Precursor by Chemical Vapor Deposition, *Chem. Mater.*, 2001, **13**(2), 588–593, DOI: 10.1021/cm001041x.

35 H. Wang, F.-X. Yin, B.-H. Chen, X.-B. He, P.-L. Lv, C.-Y. Ye and D.-J. Liu, ZIF-67 Incorporated with Carbon Derived from Pomelo Peels: A Highly Efficient Bifunctional Catalyst for Oxygen Reduction/Evolution Reactions, *Appl. Catal., B*, 2017, **205**, 55–67, DOI: 10.1016/j.apcatb.2016.12.016.

36 Y. Zhang, Y. Zhang, D. Zhang, S. Li, C. Jiang and Y. Su, Confinement Preparation of Au Nanoparticles Embedded in ZIF-67-Derived N-Doped Porous Carbon for High-Performance Detection of Hydrazine in Liquid/Gas Phase, *Sens. Actuators, B*, 2019, **285**, 607–616, DOI: 10.1016/j.snb.2019.01.105.

37 S. Li, K. Rong, X. Wang, C. Shen, F. Yang and Q. Zhang, Design of Carbon Quantum Dots/CdS/Ta3N5 S-Scheme Heterojunction Nanofibers for Efficient Photocatalytic Antibiotic Removal, *Acta Phys.-Chim. Sin.*, 2024, **40**(12), 2403005, DOI: 10.3866/PKU.WHXB202403005.

38 Y. Si, X. Li, G. Yang, X. Mie and L. Ge, Fabrication of a Novel Core–Shell CQDs@ZIF-8 Composite with Enhanced Photocatalytic Activity, *J. Mater. Sci.*, 2020, **55**(27), 13049–13061, DOI: 10.1007/s10853-020-04909-8.

39 S. Singla, P. Devi and S. Basu, Highly Effectual Photocatalytic Remediation of Tetracycline under the Broad Spectrum of Sunlight by Novel BiVO4/Sb2S3 Nanocomposite, *Catalysts*, 2023, **13**(4), 731, DOI: 10.3390/catal13040731.

40 S. Verma, B. Tirumala Rao, J. Jayabalan, S. K. Rai, D. M. Phase, A. K. Srivastava and R. Kaul, Studies on Growth of Au Cube-ZnO Core-Shell Nanoparticles for Photocatalytic Degradation of Methylene Blue and Methyl Orange Dyes in Aqueous Media and in Presence of Different Scavengers, *J. Environ. Chem. Eng.*, 2019, **7**(4), 103209, DOI: 10.1016/j.jece.2019.103209.

41 Y. Nosaka and A. Nosaka, Understanding Hydroxyl Radical (•OH) Generation Processes in Photocatalysis, *ACS Energy Lett.*, 2016, **1**(2), 356–359, DOI: 10.1021/acsenergylett.6b00174.

42 S. Khan, T. Noor, N. Iqbal and L. Yaqoob, Photocatalytic Dye Degradation from Textile Wastewater: A Review, *ACS Omega*, 2024, **9**(20), 21751–21767, DOI: 10.1021/acsomega.4c00887.

43 C. Wang, K. Rong, Y. Liu, F. Yang and S. Li, Carbon Quantum Dots-Modified Tetra (4-Carboxyphenyl) Porphyrin/BiOBr S-Scheme Heterojunction for Efficient Photocatalytic Antibiotic Degradation, *Sci. China Mater.*, 2024, **67**(2), 562–572, DOI: 10.1007/s40843-023-2764-8.

44 S. Li, R. Li, K. Dong, Y. Liu, X. Yu, W. Li, T. Liu, Z. Zhao, M. Zhang, B. Zhang and X. Chen, Self-Floating Bi4O5Br2/P-Doped C3N4/Carbon Fiber Cloth with S-Scheme Heterostructure for Boosted Photocatalytic Removal of Emerging Organic Contaminants, *Chin. J. Catal.*, 2025, **76**, 37–49, DOI: 10.1016/S1872-2067(25)64780-2.

45 D. Ma, Q. Xue, Y. Liu, F. Liang, W. Li, T. Liu, C. Zhuang, Z. Zhao and S. Li, Manipulating Interfacial Charge Redistribution in Mn0.5Cd0.5S/N-Rich C3N5 S-Scheme Heterojunction for High-Performance Photocatalytic Removal of Emerging Contaminants, *J. Mater. Sci. Technol.*, 2026, **243**, 265–274, DOI: 10.1016/j.jmst.2025.05.011.

46 S. Sadiq, I. Khan, M. Humayun, P. Wu, A. Khan, S. Khan, A. Khan, S. Khan, A. F. Alanazi and M. Bououdina, Synthesis of Metal–Organic Framework-Based ZIF-8@ZIF-67 Nanocomposites for Antibiotic Decomposition and Antibacterial Activities, *ACS Omega*, 2023, **8**(51), 49244–49258, DOI: 10.1021/acsomega.3c07606.

47 X. Zou, C. Li, L. Wang, W. Wang, J. Bian, H. Bai and X. Meng, Enhanced Visible-Light Photocatalytic Degradation of Tetracycline Antibiotic by 0D/2D TiO2(B)/BiOCl Z-Scheme Heterojunction: Performance, Reaction Pathways, and Mechanism Investigation, *Appl. Surf. Sci.*, 2023, **630**, 157532, DOI: 10.1016/j.apsusc.2023.157532.

48 P. Koundle, N. Nirmalkar, M. Momotko, S. Makowiec and G. Boczkaj, Tetracycline Degradation for Wastewater Treatment Based on Ozone Nanobubbles Advanced Oxidation Processes (AOPs) – Focus on Nanobubbles Formation, Degradation Kinetics, Mechanism and Effects of Water Composition, *Chem. Eng. J.*, 2024, **501**, 156236, DOI: 10.1016/j.cej.2024.156236.

49 S. Wu, H. Hu, Y. Lin, J. Zhang and Y. H. Hu, Visible Light Photocatalytic Degradation of Tetracycline over TiO2, *Chem. Eng. J.*, 2020, **382**, 122842, DOI: 10.1016/j.cej.2019.122842.

50 J. Wang and X. Guo, Adsorption Isotherm Models: Classification, Physical Meaning, Application and Solving Method, *Chemosphere*, 2020, **258**, 127279, DOI: 10.1016/j.chemosphere.2020.127279.

51 M. A. Al-Ghouti and D. A. Da'ana, Guidelines for the Use and Interpretation of Adsorption Isotherm Models: A Review, *J. Hazard. Mater.*, 2020, **393**, 122383, DOI: 10.1016/j.jhazmat.2020.122383.

52 A. A. Inyinbor, F. A. Adekola and G. A. Olatunji, Kinetics, Isotherms and Thermodynamic Modeling of Liquid Phase Adsorption of Rhodamine B Dye onto Raphia Hookerie Fruit Epicarp, *Water Resour. Ind.*, 2016, **15**, 14–27, DOI: 10.1016/j.wri.2016.06.001.

53 P. Sethi, S. Barman and S. Basu, Strategic Tuning of GO Ratios in CuBTC-GO Nanocomposites for next-Generation Tetracycline Adsorption: A Deep Dive into Isotherms, Kinetics, and Thermodynamics, *Sep. Purif. Technol.*, 2025, **361**, 131311, DOI: 10.1016/j.seppur.2024.131311.

54 D. Liu, Z. Huang, M. Li, X. Li, P. Sun and L. Zhou, Construction of Magnetic Bifunctional β-Cyclodextrin Nanocomposites for Adsorption and Degradation of Persistent Organic Pollutants, *Carbohydr. Polym.*, 2020, **230**, 115564, DOI: 10.1016/j.carbpol.2019.115564.

55 H. Qiu, L. Lv, B. Pan, Q. Zhang, W. Zhang and Q. Zhang, Critical Review in Adsorption Kinetic Models, *J. Zhejiang Univ. Sci. A*, 2009, **10**(5), 716–724, DOI: 10.1631/jzus.A0820524.

56 Y. S. Ho and G. McKay, Pseudo-Second Order Model for Sorption Processes, *Process*, 1999, **34**(5), 451–465, DOI: 10.1016/S0032-9592(98)00112-5.

57 P. Sethi, S. Basu and S. Barman, Innovative CuBTC/g-C3N4 Materials for Tetracycline Mitigation: Adsorption, Photocatalysis, and Mechanistic Perspectives, *New J. Chem.*, 2025, **49**(20), 8454–8471, DOI: 10.1039/d5nj00556f.

58 Y. M. Hunge, A. A. Yadav, S.-W. Kang and H. Kim, Photocatalytic Degradation of Tetracycline Antibiotics Using Hydrothermally Synthesized Two-Dimensional Molybdenum Disulfide/Titanium Dioxide Composites, *J. Colloid Interface Sci.*, 2022, **606**, 454–463, DOI: 10.1016/j.jcis.2021.07.151.

59 S. Zeinali Heris, M. Etemadi, S. B. Mousavi, M. Mohammadpourfard and B. Ramavandi, Preparation and Characterizations of TiO2/ZnO Nanohybrid and Its Application in Photocatalytic Degradation of Tetracycline in Wastewater, *J. Photochem. Photobiol., A*, 2023, **443**, 114893, DOI: 10.1016/j.jphotochem.2023.114893.

60 S. Adhikari, H. H. Lee and D.-H. Kim, Efficient Visible-Light Induced Electron-Transfer in z-Scheme MoO3/Ag/C3N4 for Excellent Photocatalytic Removal of Antibiotics of Both Ofloxacin and Tetracycline, *Chem. Eng. J.*, 2020, **391**, 123504, DOI: 10.1016/j.cej.2019.123504.

61 F. Guo, W. Shi, H. Wang, M. Han, W. Guan, H. Huang, Y. Liu and Z. Kang, Study on Highly Enhanced Photocatalytic Tetracycline Degradation of Type ‖ AgI/CuBi2O4 and Z-Scheme AgBr/CuBi2O4 Heterojunction Photocatalysts, *J. Hazard. Mater.*, 2018, **349**, 111–118, DOI: 10.1016/j.jhazmat.2018.01.042.

62 C. Maggu, S. Singla and S. Basu, Unleashing the Power of Sunlight: Bi2O3/Sb2S3 Photocatalysis for Sustainable Wastewater Remediation of Tetracycline and Rhodamine-B, *J. Environ. Manage.*, 2024, **349**, 119424, DOI: 10.1016/j.jenvman.2023.119424.

63 X. Wang, Y. Xie, J. Ma and P. Ning, Facile Assembly of Novel G-C3N4@expanded Graphite and Surface Loading of Nano Zero-Valent Iron for Enhanced Synergistic Degradation of Tetracycline, *RSC Adv.*, 2019, **9**(59), 34658–34670, DOI: 10.1039/c9ra06620a.